Title

Electron scattering processes: fundamentals, challenges, advances, and opportunities

Journal

The European Physical Journal D, 76(10)

ISSN

1155-4312

Authors

Ptasinska, Sylwia

Varella, Marcio T do N

Khakoo, Murtadha A

et al.

Publication Date

2022-10-01

DOI

10.1140/epjd/s10053-022-00482-8

Peer reviewed

Electron Scattering Processes: Fundamentals, Challenges, Advances, and Opportunities

Sylwia Ptasinska,[1,2] Marcio T. do N. Varella,[3] Murtadha A. Khakoo,[4] Daniel S. Slaughter,[5] and Stephan Denifl[6]*

[1]*Radiation Laboratory, University of Notre Dame, Notre Dame, IN 46556, USA*

[2]*Department of Physics, University of Notre Dame, Notre Dame, IN 46556, USA*

[3]*Instituto de Física, Universidade de São Paulo, Rua do Matão 1731, 05508-090 São Paulo, Brazil*

[4]*Department of Physics, California State University, Fullerton, California 92831, USA*

[5]*Chemical Sciences Division, Lawrence Berkeley National Laboratory, 1 Cyclotron Road, Berkeley, California 94720, USA*

[6]*Institut für Ionenphysik und Angewandte Physik and Center for Molecular Biosciences, Universität Innsbruck, Technikerstraße 25, 6020 Innsbruck, Austria*

[*]corresponding author: sptasins@nd.edu

Abstract

Much effort has been devoted to describing qualitatively and quantitatively electron scattering processes due to their ever-increasing importance in many industrial and medical applications. We present achievements made in the last years, focusing on some of the advancements and recent progress in the field. Particular reference is made on concrete case studies to probe the level of accord in cross-section data obtained from experiments and theory, as well as on selected instrumentation developments to probe dynamics of dissociative processes induced by electron impact. We stress that the purpose of this colloquium paper is not to be a comprehensive review but rather to provide a snapshot of different research topics in electron scattering by pointing out certain challenges and, therefore, indicating opportunities to facilitate further experimental and theoretical work.

1. Introduction

Over the past several decades, significant efforts of the atomic and molecular physics community have been directed to achieve an in-depth and complete understanding of electron scattering processes with diverse targets, ranging from atoms to polyatomic systems, including clusters. Electron-target interactions are involved in a plethora of physicochemical processes because low-energy electrons (LEEs) are one of the most abundant products of ionizing radiation and terrestrial and human-made plasma discharges. Moreover, these free and quasi-free LEEs are also present naturally in cellular systems, and thus are involved in biochemical transfer reactions, or in the atmosphere and surface of astronomical objects, and are crucial to manufacture materials and operate electronic, electrochemical, and photovoltaic devices in industrial use. However, before obtaining a comprehensive knowledge of LEEs' roles and exploiting their full potential in both natural and artificial processes, experimental and theoretical studies of electron scattering are required to achieve both goals. In particular, a detailed description of collisional processes that occur between an isolated atom, molecule, or cluster with an incident electron is the first step in providing our understanding of collective phenomena in more complex systems.

In general, during collisions, LEEs can be scattered elastically or inelastically, leading to rotational, vibrational, and electronic excitation or dissociation of the target molecule. Possible dissociative processes include neutral dissociation (referred to also as direct dissociation or dissociative excitation), dissociative ionization, including both electron impact ionization and ion-pair formation, and dissociative electron attachment (DEA). The fragments formed in the dissociative processes can possess an unbalanced charge in their structure or have relatively high kinetic energy; thus, they can be involved in other secondary processes upon interaction with any surrounding environment. Therefore, characterization of the target's final state or the final products of dissociation is essential not only for our fundamental understanding of the energetics and dynamics in electron-molecule interactions, but also reactivity and chemical specificity that can be important for physical and chemical transformations driven by LEEs.

In addition to identifying the types of processes involved in an electron collision with the target, their cross-sections are most critical quantities that represents the collision probabilities of scattering. However, despite substantial technical progress in measuring cross-sections accurately, it is still difficult to determine absolute cross-sections for the scattering processes because of limited ability to measure important parameters in the interaction region precisely. Thus, the electron collisional cross-sections measured for a target under investigation are normalized and related to those for which the absolute cross-sections have been determined. In parallel, the advancement in computational technology has allowed better theoretical models to be developed that have been able to provide qualitative explanations of the data observed or even to reproduce and predict them quantitatively.

A rich body of literature is dedicated to the fundamentals of gas-phase scattering processes at electron impact energies below 100 eV. These have provided a great deal of information on collisional phenomena, their types, cross-sections, and final states and products. This colloquium paper reports only the current status of several selected topics in this field, with a particular focus on the experimental and computational challenges that remain, and the potential opportunities to extend existing experimental and theoretical methodologies to advance our understanding. The close and frequent interplay between experiment and theory has been demonstrated throughout the years to be a determining force in improving the precision of experimental studies, and enhancing and providing novel theoretical models to identify the observed data correctly. Further, it has been necessary to validate and confirm theoretical hypotheses and assumptions based upon experiments. Therefore, this colloquium paper discusses first the current status of theoretical methods in electron-target scattering briefly, with a particular focus on the DEA process. This section is followed by recent examples of the intersection between theoretical and experimental cross-sections for atoms, and diatomic and polyatomic molecules, including angle-differential electron scattering cross-sections. Before the final section, which summarizes emerging work in the atomic and molecular physics community and suggests potential future research, three recent advancements in experimental capabilities are presented. It is important to stress that these developments in instrumentation are still ongoing; therefore, although only a limited number of research studies is presented here, they include concrete examples with a brief outlook of their possibilities for future efforts. However, they have proven to be significant already as they have revealed novel aspects in electron collisional phenomena that were inaccessible previously due to technical limitations.

In addition, the selection of these three instrument developments in this colloquium paper is attributable to the need to understand electron-initiated processes better in complex environments, including condensed matter. Therefore, to achieve this, the knowledge of the dynamics and reactivity of products formed because of dissociation upon electron-target collision is essential first. Hence, the instrumentation advancements presented here consider largely the processes that involve electron capture and lead to DEA or inter-Coulombic processes. We describe here experimental progress in measurements of kinetic energy and angular distribution of atomic and molecular fragments, and detection of neutral fragments. Moreover, to approach our understanding of electron scattering in media, particularly the hydration effect, one of the designs of the cluster apparatus dedicated for DEA is also presented. The example of hydrated radiosensitizers was chosen because such work carries not only fundamental importance, but is related to the application of electron scattering processes in other research areas as well. Thus, the purpose of this colloquium paper is to provide recent experimental and theoretical findings and developments as well as their intersection in selected topics in the area of electron-target scattering.

2. Theory of Electron-Molecule Scattering and Dissociative Electron Attachment

Various computational methods have been adopted to calculate electron-target scattering cross-sections. In this section, we focus on a brief description of the basis of electron scattering theory and emphasize novel developments in DEA modeling.

2.1 Electron scattering theory

Electronic structure techniques, such as quantum chemistry (QC) methods, have always challenged the available numerical capabilities. If we consider the Roothan's seminal work as the milestone for contemporary QC algorithms [1], the remarkable progress achieved in both hardware and software developments over six decades is unquestionable. Nevertheless, the ever-increasing sophistication of QC techniques, as well as the size and complexity of the physicochemical systems of interest, often encounter numerical limits.

Scattering problems pose an even more stringent challenge to method development and computational capability. Essentially, all of the difficulties in describing molecular bound states, e.g., accounting for electronic correlation, are also found in LEEs' interactions with molecules. However, even in elastic collisions, the delocalized character of the scattering wave function makes the numerical solutions inherently more difficult in comparison to a QC method of similar quality. Keeping the nuclei with fixed positions, neglecting ionization, and omitting spin degrees of freedom for simplicity, the asymptotic condition for electron scattering by an *N*-electron molecular target can be written as:

$$\Psi_{\vec{k}_i}^{\iota\iota\iota}.$$

Equation (1)

in the expression above, $\Psi_{\vec{k}_i}^{\iota\iota\iota}$ is the scattering wave function with the outgoing boundary condition, $\vec{k}_i$ ($\vec{k}_f$) is the projectile incident (outgoing) wave vector, $\vec{r}_n$ are electronic coordinates ($n=1,\cdots,N+1$), and Φ_f are target electronic states, in which $f=0$ is the ground state and assumed to be the initial state. In the second term on the right-hand side, the spherical wave is modulated by the scattering amplitude $f\left(\vec{k}_f,\vec{k}_i\right)$.

Several computational methods have been proposed to calculate electron scattering amplitudes. While a comprehensive review of those methods is beyond the scope of this colloquium paper, some of the approaches available are outlined below. Typically, the many-body methods are applied to low-energy collisions, in which the ionization channels can be neglected. The projectile and target electrons are treated explicitly through anti-symmetric wave functions, and there are basically three methods of this kind. The complex Kohn method is based on the Hultén-Kohn variational principle for the Schrödinger equation, which can only be satisfied if the trial wave function has the correct asymptotic behavior [2]. The Schwinger Multichannel (SMC) method is built on the Schwinger variational principle for the integral Lippmann-Schwinger equation, which incorporates the scattering boundary condition through the free-particle Green's function [3]. Finally, the R-matrix method is based formally on the continuity of the logarithmic derivative of the wave function on a boundary that defines inner and outer regions [4]. The R-

matrix amplitudes, which are related to the logarithmic derivative, are obtained from the solution of a modified variational problem in the inner region. The amplitudes can be connected to the K-matrix (and hence the scattering amplitude) in the outer region. The three methods use trial wave functions given by:

$$\Psi_{\vec{k}_i}^{\dot{\iota}\dot{\iota}} ,$$

Equation (1)

in which $c_{\mu\nu}$ are variational coefficients, Φ_μ is a target state, φ_ν is either a localized or scattering orbital, and the operator A imposes the proper anti-symmetrization conditions on the target wavefunction. Apart from the need to describe the electronic states of the target molecule, which can be a numerically intensive problem itself, the many-body scattering methods require additional costly computational steps to account for the appropriate boundary conditions.

Given the significant numerical effort the many-body methods require, several types of single-body methods have been proposed. Typically, these employ model potentials to account for exchange and correlation-polarization effects, such that only one electron (the projectile) is explicitly described in the solution. Representative examples include symmetry-adapted single-center expansions [5], the momentum-space representation [6], and the Schwinger variational iterative method (SVIM) [7]. In addition, the model potential sometimes incorporates an imaginary component that accounts for inelastic effects, such as electronic excitation and ionization [8]. The imaginary potentials, which absorb part of the scattering flux from the elastic channel, are also employed in multiple scattering methods. In this third class of methods, the scattering amplitudes for electron-molecule collisions are derived from an expansion over electron-atom amplitudes. Representative examples are the independent atom model with screening-corrected additivity rule (IAM-SCAR) [9] and the spherical complex optical potential (SCOP) method [10].

Frequently, the solution of electron scattering problems is concerned with the characterization of resonances, i.e., temporary molecular anions (TMAs) also referred as transient negative ions, formed by electron attachment to the target atom or molecule. A resonance is unstable against auto-ionization and can be described by complex energies. The real part corresponds to the anion energy relative to the isolated neutral target, while the imaginary part is related to the auto-ionization lifetime. The formation of resonance gives rise to a cross-section peak, ideally with Lorentzian shape, in which the energy position and width indicate the real and imaginary components of the TMA resonance, respectively. This information can also be obtained with modified QC (MQC) methods [11], which resort to the complex scaling of the electronic coordinates or complex absorbing potentials to estimate the resonance energies. Finally, even conventional QC methods can be used to describe resonances, although a series of calculations for each anionic state must be performed to generate a stabilization graph. By varying a certain parameter that represents an effective box size (e.g., rescaling the basis set exponents), the

complex energies are estimated from avoided crossings between resonance and discretized continuum states [12].

2.2 DEA models

The relevance of electron-molecule resonances in chemical processes is related closely to the dissociation of the TMAs, a process referred to as DEA [13]. The formation of the anion can be viewed as rapid on the time scale of molecular vibrations, i.e., as a sudden change in the potential energy surface (PES) that triggers the vibration dynamics on the complex potential. As the additional electron can occupy anti-bonding orbitals, and molecular moieties with high electron affinities are likely to give rise to anionic fragments, the TMA may dissociate. However, the DEA channels always compete with other processes, e.g., auto-ionization; therefore, it is important to describe the real and imaginary parts of the complex potential accurately. From the theoretical standpoint, the need to account for the imaginary part of the energy is a fundamental aspect that may be clarified by an analogy with photon-induced excited state dynamics. Similarly, photon absorption changes the PES suddenly and initiates vibration dynamics. Further, the excited electronic states are also transient, unstable against spontaneous emission, and thus can be described by complex energies. Finally, ultrafast internal conversion processes occur frequently in both DEA and excited-state dynamics and should be taken into account.

Nevertheless, a fundamental distinction between the electron- and photon-induced unimolecular reactions arises from the different lifetime scales. The spontaneous emission width (Γ_e), which accounts for the coupling with the continuum of matter-radiation states, can be neglected safely in most applications to molecular systems because the related lifetimes ($\hbar/\Gamma_e$) are very long on the ultrafast time scale. On the other hand, the auto-ionization widths (Γ_a) that account for the coupling to the continuum of auto-ionization states, are much larger than their spontaneous emission counterparts. Typically, the auto-ionization related lifetimes ($\hbar/\Gamma_a$) are on the femtosecond scale and cannot be disregarded along the DEA dynamics.

The description of complex potentials is even more challenging than it may sound at first. The electron attachment amplitude has a non-local dependence on the collision energy and nuclear coordinates [14]. These non-local effects have been observed experimentally in several small molecules [15-17] and even in more complex biomolecular targets such as uracil [18]. The non-local character poses difficulties to the representation of the complex potential in the energy domain, and also implies non-Markovian dynamics in the time domain. Although the Feshbach projection operator (FPO) [14] and the vibrational R-matrix [19,20] approaches can account for non-locality in resonant vibrational excitation and DEA, those effects make the computational description of the TMA state dynamics a formidable task. Consequently, many applications resort to the local approximation [14], which amounts to a complex PES in the Born-Oppenheimer sense, $V(\vec{R}) = E_{\mathrm{res}}(\vec{R}) - (i/2)\Gamma(\vec{R})$, in which $\vec{R}$ denotes the nuclear coordinates collectively. Despite being less demanding than non-local approaches, the local approximation is

still highly labor-intensive and time-consuming because a reasonable description of the complex potential surface requires scattering or MQC computations to be performed for many different geometries.

Although a comprehensive review of the literature on DEA simulations is beyond the scope of this colloquium paper, we mention a recent review [13] and several representative examples that may serve as a guide for the interested reader. The early efforts and theoretical developments that explored the FPO approach have been reviewed [14,21], and more recent applications have focused on non-local effects [16,17,22]. In addition, FPO-based models have been combined with the complex Kohn scattering method in several studies, including the classic work on DEA to water [23-25] and the simulations of momentum imaging data [26]. In other works, the R-matrix methodology was applied to a remarkable variety of systems, ranging from diatomic molecules to clusters [18,20,27,28]. However, because of the numerical challenges outlined above, computational models for DEA dynamics are often restricted to a few vibrational modes, typically ≤ 3, i.e., in diatomic and triatomic molecules, or reduced-dimensionality models for polyatomic systems.

2.3 On-the-fly DEA dynamics

Time-dependent approaches to DEA dynamics have long been proposed [14]. In several applications, the complex-Kohn scattering method was employed to compute complex PESs [23-25] on which vibrational wave packet dynamics were calculated with the multi-component time-dependent Hartree (MCTDH) method [29], which is applied routinely to photo-induced dynamics. Classical [30-32] and semiclassical [33] propagation methods have been employed also, but the need to compute the complex PESs, and possibly non-adiabatic couplings, remains a numerical challenge. The high dimensionality of the PESs can be a severe limitation in photochemical and photophysical problems as well, despite the use of real-valued potentials. Nevertheless, the simulation of excited-state dynamics has advanced substantially in the last decades. The progress was attributable to a significant extent to on-the-fly methods for molecular dynamics. In this approach, the nuclei are time-evolved classically (or semiclassically) under forces obtained from the gradients of the electronic energies computed with QC methods. The electronic energies and gradients need to be computed only along the classical trajectories, which reduces the computational effort considerably in comparison to that for vibrational dynamics calculations on pre-computed PESs. The mixed quantum-classic (MxQC) on-the-fly techniques can also account for nuclear quantum effects, in particular non-adiabatic transitions, without a prohibitive increase in the numerical burden [34]. While several types of these methodologies have been proposed, we focus here on the trajectory surface hopping (TSH) [35,36] and *ab initio* multiple spawning (AIMS) [37] methods, as these have been used recently in DEA simulations [38-40].

2.3.1. Surface hopping

The basic goal of TSH is to propagate a swarm of classical trajectories to mimic a vibrational wave packet. Each trajectory evolves typically on a given adiabatic PES, but non-adiabatic transitions are introduced with a stochastic algorithm that allows trajectory hopping, i.e., once the trajectory reaches some PES region where significant non-adiabatic couplings are found, it may change from one coupled potential surface to the other along the dynamics. Therefore, the hopping can emulate the quantum population transfer (e.g., internal conversion) among the electronic states. For example, if a two-state problem is assumed with all trajectories in the same PES initially, some trajectories will remain on that potential surface at the end of the propagation, while others will have hopped to the other electronic state. A discussion of the technical and more advanced aspects of the TSH method can be found elsewhere [34,41], but the basic equations are as follows. The time-dependent wave function is written as:

$$\psi(\vec{r},\vec{R},t)=\sum_j c_j(t)\Phi_j(\vec{r};\vec{R}(t)),$$

Equation (3)

in which $\vec{r}$ and $\vec{R}$ denote the coordinates of the electrons and classical nuclei, respectively. The electronic states $\Phi_j(\vec{r};\vec{R}(t))$ depend parametrically on the nuclear coordinates, as indicated by the semicolon, and the coefficients $c_j(t)$ can be viewed as time-dependent population amplitudes. By substituting the wave function ansatz in the molecular time-dependent Schrödinger equation, and projecting onto the k-th electronic state, one obtains a set of coupled equations for the coefficients (atomic units are henceforth used):

$$i\frac{d}{dt}c_k(t)=\sum_j\left(\delta_{kj}V_k-i\vec{F}_{kj}\cdot\vec{v}\right)c_j(t),$$

Equation (4)

in which the electronic states are assumed to be adiabatic and orthonormal. In the expression above, V_k is an adiabatic PES, $\vec{v}$ is the vector of classical nuclear velocities, and $\vec{F}_{kj}=\langle\Phi_k|\nabla_{\vec{R}}|\Phi_j\rangle$ is the non-adiabatic coupling vector (integration over the electronic coordinates is implied in the bracket). For any given trajectory, the nuclei are time-evolved classically with forces provided by the gradient of the adiabatic PES at their instantaneous positions, $\vec{f}_l=-\nabla_{\vec{R}}V_l$, in which the l-th potential surface is assumed to be the current electronic state. According to Eq. (4), the other electronic states, $j\neq l$, can acquire non-zero amplitudes because of the non-adiabatic couplings. The fewest-switches algorithm proposed in an earlier work [36], which minimizes the number of hopping events in one time step, Δt, is the procedure employed most widely to account for population transfer. The hopping probability of the $l\rightarrow k$ transition corresponds to the ratio [increment in the k-th state population because of the flux from l in the time step Δt]/[l-th state population]. Mathematically, the probability is given by:

$$P_{l\to k}=\max\left[0,\frac{2\Delta t}{\rho_{\text{¿}}}\left(\mathrm{Im}\left(\rho_{kl}\right)\delta_{kl}V_l-\mathrm{Re}\left(\rho_{kl}\right)\vec{F}_{kl}\cdot\vec{v}\right)\right],$$

Equation (5)

in which the density matrix, $\rho_{kl}=c_k c_l^{\text{¿}}$, was introduced. In a given time t, the $l\to k$ hopping takes place if:

$$\sum_{n=1}^{k-1}P_{l\to n}(t)<r\le\sum_{n=1}^{k}P_{l\to n}(t),$$

Equation (6)

in which $r\in[0,1]$ is a uniformly chosen random number, and a second condition prevents total energy increases in the hopping event. Once a trajectory hops, the nuclear momenta are rescaled along the direction of the coupling to enforce energy conservation [41].

The fewest-switches surface hopping (FSSH) technique outlined above was adapted recently to DEA problems [38,39]. The Wigner distribution of the neutral molecule is denoted as $W(\vec{x})$, in which $\vec{x}=(\vec{R}_0,\vec{p}_0)$ is a point in the nuclear phase space with coordinates $\vec{R}_0$ and momenta $\vec{p}_0$. Assuming that the resonance is formed as the projectile kinetic energy matches the local-approximation vertical resonance position, $E_{\text{res}}(\vec{R}_0)$, the attachment probability can be written as,

$$p_{\text{att}}(\vec{x},E)\,d\vec{x}=\Gamma\left(\vec{R}_0,E\right)\delta\left[E-E_{\text{res}}\left(\vec{R}_0\right)\right]W(\vec{x})\,d\vec{x},$$

Equation (7)

in which E is the energy of the incident electron, and $\Gamma\left(\vec{R}_0,E\right)$ is the non-local (energy-dependent) resonance width, which can be related to the local-approximation width, $\Gamma_L(\vec{R}_0)=\Gamma(\vec{R}_0,E_{\text{res}}(\vec{R}_0))$. Once the TMA is formed, the nuclear coordinates evolve classically, $\vec{R}(\vec{x},t)$, where the dependence on the initial condition $\vec{x}$ is indicated explicitly. Following previous work [31], the survival probability, which is the probability that auto-ionization has not taken place up to time t, is written as

$$p_{\text{surv}}(\vec{x},t)=\exp\left(-\int_0^t\Gamma_L(\vec{R}(\vec{x},t'))\,dt'\right).$$

Equation (8)

The survival probability decreases from $p_{\text{surv}}(0)=1$, in which $t=0$ is the attachment time, although it does not vanish necessarily, as the width reaches zero in the case when the anion becomes stable with respect to the neutral molecule. Therefore, at sufficiently long times, the probability tends toward a constant value, either zero or finite, and depends only on the initial

conditions, $p_{\mathrm{surv}}(\vec{x}, t \to \infty) \equiv p_{\mathrm{surv}}(\vec{x})$. Essentially, the phase-space integration of the product $p_{\mathrm{att}} \times p_{\mathrm{surv}}(\vec{x})$ gives the DEA cross-section:

$$\sigma(E) = \frac{\pi}{E} \int \Gamma\left(\vec{R}_0, E\right) \delta\left[E - E_{\mathrm{res}}\left(\vec{R}_0\right)\right] p_{\mathrm{surv}}(\vec{x})\, W(\vec{x})\, d\vec{x}.$$

Equation (9)

In practice, the integration is performed as an average over a discrete set of initial conditions sampled according to the Wigner distribution. The local width is employed to compute the survival probability along the trajectories, but the energy dependence is kept in the attachment probability:

$$\Gamma\left(\vec{R}, E\right) \approx \Gamma_L\left(\vec{R}\right) \frac{\gamma(E)}{\gamma\left(E_{\mathrm{res}}\left(\vec{R}\right)\right)}.$$

Equation (10)

The energy-dependent term $\gamma(E)$ is used to impose the Wigner threshold law (WTL), which improves the near-threshold behavior of the DEA cross-section [14,21]. The expression above can be viewed as a semi-local approximation [14,42], in the sense that the energy dependence is accounted for in the attachment process, while the nuclear dynamics is considered on the local PES of the transient anion state. The working expression for the cross-section is:

$$\sigma(E) = \left(\frac{\pi}{E}\right) \frac{1}{N} \sum_{i=1}^{N} \frac{\gamma(E)}{\gamma\left(E_{\mathrm{res}}\left(\vec{R}_0^i\right)\right)} \Gamma_L\left(\vec{R}_0^i\right) g_l\left(\vec{R}_0^i, E\right) p_{\mathrm{surv}}\left(\vec{x}^i\right),$$

Equation (11)

in which the sum runs over the set of *N* initial conditions. The phenomenological broadening function $g\left(\vec{R}_0^i, E\right)$, assumed to have a Lorentzian shape, is similar to those employed in photoabsorption cross-sections calculated with the nuclear ensemble method [43]. The broadening smooths out the energy dependence of $\sigma(E)$, thus avoiding a prohibitively large number of initial conditions, and hence, trajectories.

The MxQC method for DEA dynamics, which assumes a single resonance state, works in practice as follows. Once the initial conditions are sampled, the trajectories are propagated on the (local-approximation) real part of the PES, $E_{\mathrm{res}}(\vec{R})$, while the imaginary part, $\Gamma_L(\vec{R})$, is used to integrate the survival probability. Therefore, the local complex potential surface should be computed for every position in all trajectories until $p_{\mathrm{surv}}(t)$ converges to the final constant value. This procedure would be very time-consuming, if not impractical, with either scattering, MQC or stabilization methods. Therefore, the most stringent approximations, which are justified as a means to avoid the prohibitively large numerical effort, are (i) to employ standard QM methods

to estimate $E_{\mathrm{res}}(\vec{R})$, and (ii) to build a model for the geometry dependence of $\Gamma_L(\vec{R})$ from as few as possible scattering, MQC or stabilization calculations. The first approximation is reasonable for narrow resonances, while the second depends on the reaction pathways.

As a first application of the MxQC method, DEA to chloroethane (CH_3CH_2Cl) was considered, specifically the formation of Cl^- fragments on the complex potential of the σ^* shape resonance [38]. This choice was convenient, as a single resonance is relevant to the dissociation reaction, in which the C–Cl bond length is the reaction coordinate. While we do not discuss the technical details of the model, we mention briefly that the real part of the complex potential was described with the multi-reference configuration interaction method, with singles and doubles excitation (MRCISD), in addition to numerical tests performed with lower-level methods. The MRCISD potential was shifted uniformly to match the resonance position computed with the SMC method at the neutral molecule's optimal geometry [3]. The local width was modeled as a function of the resonance position, $\Gamma_L(\vec{R})=\Gamma_L(E_{\mathrm{res}}(\vec{R}))$ obtained from a polynomial interpolation of SMC calculations performed for four C–Cl bond lengths, and then applied to all geometries accessed along the dynamics. Finally, the energy-dependent term of the attachment probability, $\gamma(E)$, was computed from the least-squares fit of a model form, consistent with the WTL for the s wave, to eigenphase sums computed with the SMC method (at the optimal geometry of the neutral target molecule).

It is worth stressing that the MxQC dynamics were performed in full dimensionality, i.e., taking all of the vibrational modes into account. Although not shown here, four internal coordinates were activated strongly along the DEA reaction of the CH_3CH_2Cl molecule; specifically, the C–Cl bond length, which can be viewed as the reaction coordinate that produces the Cl^- fragment, the C–C bond length, the C–C–Cl angle, and the H_2C–C pyramidalization angle. The DEA cross-sections calculated are shown in Fig. 1, together with the experimental data [44]. In panel (a), the cross-sections were computed with 100 and 1400 trajectories, employing a phenomenological linewidth of 0.1 eV (see Eq. (11)). The results shown in panel (b) were obtained with the same numbers of trajectories, although with broader linewidths of 0.5 eV. The structures in panel (a) are unphysical, and merely reflect the poor statistical convergence of the calculation performed with only 100 trajectories. Those structures are removed by the broader linewidth (panel (b)), but even the worst result (dashed line in panel (a)) can be considered reasonable. Apart from the unphysical oscillations, the nature of which is understood well, the energy dependence of the cross-section is consistent with the data because the DEA peak position (approximately 1.5 eV) is displaced with respect to the vertical resonance position (2.33 eV). The number of trajectories and the broadening affect the cross-section magnitude clearly, but two important aspects should be kept in mind: (i) how challenging it is to compute a DEA cross-section in full dimensionality for polyatomic systems, and (ii) most of the DEA data for polyatomic molecules, in particular small biomolecules, are not reported as normalized absolute cross-sections.

The dependence of the resonance parameters used in the model on the results was also considered. As mentioned previously, the local width was described as a function of the

resonance position at any given geometry, $\Gamma_L\left(E_{\text{res}}\left(\vec{R}\right)\right)$. **Fig. 1**(c) shows the DEA cross-sections obtained with different values for the vertical resonance position (at the optimal geometry of the neutral target), specifically at 2.23, 2.33, and 2.43 eV, while the same functional form for the width was maintained. In **Fig. 1**(d), the vertical resonance position was kept at the value obtained from SMC computations, 2.33 eV, but the vertical width was varied, i.e., 1.25, 1.35 (SMC estimate), and 1.45 eV. The latter procedure amounts to rescaling the width by a multiplicative factor for all geometries. The variation in the vertical resonance position shifts the peak position in **Fig. 1**(c), as expected, but in general, the shapes of the cross-sections calculated are fairly similar. Once more, the cross-section magnitude appears to be more sensitive to the model parameters than its energy dependence.

DEA to chloroethane can be viewed as a simple application of the MxQC framework, despite the 18 vibrational modes, as the dynamics on the complex potential of the σ^* shape resonance is adiabatic. The complex surface FSSH (CS-FSSH) method was developed to generalize the FSSH technique outlined above to complex Hamiltonians [39] and implemented in the Newton-X package [45]. While survival probabilities could also be used in non-adiabatic dynamics (see below), an interesting alternative approach was proposed, i.e., a complex Hamiltonian, which can be represented in the basis of electronic states as $\langle \Phi_j | H | \Phi_k \rangle = H^R_{jk} - (i/2)\Gamma_{jk}$ was assumed. The real part corresponds to the matrix elements found in the usual TSH approach, which are diagonal for adiabatic states, $H^R_{jk} = \delta_{jk} V_k$. The matrix elements of the imaginary part appear in Eq. (4) now, such that the time propagation is no longer unitary, i.e., $\sum_n |c_n(t)|^2 < 1$. The DEA cross-section, Eq. (11), is then expressed elegantly in terms of the final populations of the electronic states, and the transition probability, Eq. (5), is also modified to incorporate the Γ_{jk} matrix elements. The formalism is general, in the sense that it can be applied to any open system described by a complex Hamiltonian, but the first application concerned the adiabatic and non-adiabatic DEA dynamics of iodoethene (C_2H_3I). This molecule has two well-known resonances, a (vertically) lower-lying σ^* shape resonance with a repulsive potential surface, and a higher-lying π^* shape resonance. The formation of the repulsive σ^* state initiates an essentially adiabatic DEA dynamics, similar to that in chloroethane, while the formation of the π^* state triggers a non-adiabatic dissociation mediated by the π^*/σ^* coupling.

We will not discuss the numerical procedures of the calculations, which can be found in the original publication [39]. The dynamics were based on MRCIS potentials, and the local width models were built as outlined above for chloroethane, with SMC computations performed on a small number of geometries selected from exploratory simulations in the real-valued PESs. Finally, the off-diagonal imaginary potential couplings, Γ_{jk}, were assumed higher-order effects and neglected, such that only the diagonal elements that correspond to local resonance widths, were considered. The non-adiabatic DEA dynamics triggered by the π^* resonance was particularly rich. The C=C bond length acted as the tuning mode, driving the PESs to the crossing region. The out-of-plane motion of the hydrogen atoms was identified as the coupling coordinate, while C–I stretch was the reaction coordinate. The C=C mode was activated very

early, at approximately 5 fs, while many trajectories hopped from 5 to 15 fs. After the transitions, the electronic state developed a clearer σ^{*} character along the trajectories and led to the formation of I^- fragments. The DEA cross-section calculated is shown in Fig. 2, together with the experimental data [46]. The experimental results were not reported in absolute values, so they were normalized to the peak height calculated. Once again, the theoretical results described the energy dependence of the cross-section faithfully, i.e., the positions and relative heights of the DEA peaks near 0.25 and 1.0 eV. The contributions from both DEA mechanisms, namely adiabatic dynamics on the σ^{*} anion state surface and non-adiabatic dynamics triggered by the π^{*} state, are resolved in the right panel, showing that the lower and higher-lying DEA peaks arise from the adiabatic and non-adiabatic mechanisms, respectively.

2.3.2. Multiple spawning

The AIMS approach [37] differs from TSH in two fundamental aspects. The nuclei are propagated semi-classically, rather than classically, and the semi-classical nuclear wave packets do not hop between non-adiabatically coupled electronic potentials, but rather give rise to new wave packets (spawning). The molecular wave function is based on the Born-Huang expansion:

$$\psi\left(\vec{r},\vec{R},t\right)=\sum_{j}\chi_{j}\left(\vec{R},t\right)\Phi_{j}\left(\vec{r};\vec{R}(t)\right),$$

Equation (12)

in which the nuclear wave packets, $\chi_j(\vec{R},t)$, can be viewed as $\vec{R}$-dependent expansion coefficients, compared to the purely time dependent coefficients in Eq. (3). Those wave packets are propagated in the frozen Gaussian approximation (FGA) [47], i.e., the $\chi_j(\vec{R},t)$ functions are linear combinations of multi-dimensional traveling Gaussians:

$$\chi_{j}\left(\vec{R},t\right)=\sum_{\alpha}C_{\alpha}^{j}(t)\,\chi_{\alpha}^{j}\left(\vec{R};\vec{R}_{\alpha}^{j}(t),\vec{P}_{\alpha}^{j}(t),\gamma_{\alpha}^{j}(t),\beta_{\alpha}^{j}\right),$$

Equation (13)

in which the χ_α^j functions are given by products of one-dimensional Gaussians for the $3N_{at}$ nuclear Cartesian coordinates, in which N_{at} is the number of atoms in the molecule. Consistent with the FGA framework, the center of the Gaussians in both the position ($\vec{R}_\alpha^j$) and momentum ($\vec{P}_\alpha^j$) spaces follow classical trajectories. The exponents, (β_α^j), are kept frozen during the time propagation, while the dynamical phases, (γ_α^j), are obtained from action integrals over the classical paths. The multi-dimensional Gaussians, χ_α^j, are referred to as trajectory basis functions (TBFs), and the time evolution of the coefficients C_α^j is governed by the nuclear Schrödinger equation:

$$\frac{d}{dt}C_\alpha^j(t)=-i\sum_{\mu,\nu}\left(S_{jj}^{-1}\right)_{\mu\nu}\left[\left(H_{jj}-i\dot{S}_{jj}\right)_{\mu\nu}C_\nu^j+\sum_{k\neq j}\left(H_{jk}\right)_{\mu\nu}C_\nu^k\right].$$

Equation (14)

In the expression above, $\left(S_{jj}\right)_{\mu\nu}=\left\langle\chi_\mu^j\middle|\chi_\nu^j\right\rangle$ is a time-dependent nuclear overlap matrix and $\left(\dot{S}_{jj}\right)_{\mu\nu}=\left\langle\chi_\mu^j\middle|\left(\partial/\partial t\right)\chi_\nu^j\right\rangle$ is its time derivative. The evaluation of the nuclear overlaps and the spawning algorithm are described in detail elsewhere [37]. For the present purposes, it was observed that any given TBF is propagated adiabatically until the underlying trajectory reaches a region with significant non-adiabatic coupling, referred to as the spawning region. The TBF dwells in this region for $t_{\text{entry}}<t<t_{\text{exit}}$, and during this period, the propagation accounts for the coupled potentials, with the coupling given by $\vec{F}_{kj}\cdot\vec{v}$, as in Eq. (4). For $t>t_{\text{exit}}$, the parent TBF remains on its original potential surface, a child TBF is generated on the other surface, and probability conservation is imposed through the coefficients, $C_\alpha^j(t)$.

The AIMS method was adapted to the DEA process [40], in which a generalization of the survival probability for non-adiabatic dynamics was proposed. The working expression for the DEA cross-section is given by

$$\sigma(E)=\left(\frac{\pi}{E}\right)\frac{1}{N_{IC}}\sum_{n=1}^{N_{IC}}\Gamma\left(\vec{R}_0^n,E\right)g_l\left(\vec{R}_0^n,E\right)p_n^{\text{surv}},$$

Equation (15)

in which N_{IC} is the number of initial conditions. The attachment width, $\Gamma\left(\vec{R}_0^n,E\right)$, and the phenomenological broadening function, $g_l\left(\vec{R}_0^n,E\right)$, are the same as in Eqs. (10) and (11), respectively. The survival probability, p_n^{surv}, depends on the fragmentation channel of interest, and can be expressed in terms of the TBFs:

$$p_n^{\text{surv}}=\sum_{\lambda_n=1}^{N_{\text{TBF}}^n}\theta_{\lambda_n}^{\text{DEA}}p_{n_j}^{\text{surv}}(t\to\infty).$$

Equation (16)

N_{TBF}^n is the number of TBFs generated from the n-th initial condition, and the step function $\theta_{\lambda_n}^{\text{DEA}}$ equals one in the case when the λ_n-th TBF contributes to the DEA channel of interest, or zero otherwise. The TBF-specific survival probability, $p_{n_j}^{\text{surv}}$, is similar to that defined in Eq. (8), although the auto-ionization widths are considered according to the history of spawning events. For instance, if a child TBF that contributes to DEA on the j-th complex potential surface is assumed. In the case that TBF is generated from a parent on the k-th surface at $t=t_{\text{spawn}}$, the survival probability should be computed from the width Γ_k for $t<t_{\text{spawn}}$, while from Γ_j for $t>t_{\text{spawn}}$. The probability also depends on the final population of the j-th state and is computed assuming that the dwell time in the spawning region is negligible ($t_{\text{exit}}\approx t_{\text{entry}}$). In practice, the time propagation is governed by the real parts of the complex potentials, so the standard AIMS

algorithm can be used, while the survival probabilities are computed from the imaginary parts. The latter are obtained as functions of the resonance positions, $\Gamma_L(E_{\mathrm{res}}(\vec{R}))$, as discussed above.

The AIMS-based DEA method was applied to 5-bromo-uracil (5BrU), specifically to simulate the dynamics triggered by the formation of the $\pi_2^{\ddagger}$ resonance [40]. At the optimal geometry of the neutral target, there are four anionic states [48], i.e., a dipole-bound state (DBS), a valence bound state ($\pi_1^{\ddagger}$), and two shape resonances ($\sigma_{\mathrm{CBr}}^{\ddagger}$ and $\pi_2^{\ddagger}$). The DBS was not considered in the DEA simulations as the use of diffuse basis sets could introduce pseudo-continuum orbitals in the QC calculations. The real parts of the complex potentials of the $\pi_1^{\ddagger}$, $\sigma_{\mathrm{CBr}}^{\ddagger}$, and $\pi_2^{\ddagger}$ states were described with the floating occupation molecular orbital-complete active space configuration interaction (FOMO-CASCI) method, and employed a small active space with 3 electrons in 4 orbitals. The local width was modeled as a function of the resonance position, $\Gamma_L(\vec{R}) = \Gamma_L(E_{\mathrm{res}}(\vec{R}))$, to explore SMC calculations performed for different C_5–Br bond lengths.

According to the simulations, the decay of the $\pi_2^{\ddagger}$ shape resonance essentially gives rise to Br^- fragments. The DEA cross-section calculated behaves in much the same way as those obtained for chloroethane and iodoethene. The energy dependence is consistent with the data reported earlier [49], considering only the DEA peak that arises from the $\pi_2^{\ddagger}$ state. Further, the cross-section shape is robust with respect to reasonable variations in the model parameters, while the magnitude is more sensitive to those parameters and probably less accurate. The correct energy dependence is a remarkable result, given that only 21 initial conditions were sampled from the Wigner function of the neutral molecule, and a modest active space was employed in the FOMO-CASCI computations. The initial conditions gave rise to 122 trajectories through the spawning processes, indicating rich dynamics. Four vibrational coordinates were activated strongly, the C_5–Br and N_1–H bond lengths, out-of-plane vibrations of the Br atom, and a ring puckering angle. Because the anion states change their characters along the propagation, they are referred to as D_0, D_1, and D_2 in order of increasing energy, where it should be clear that those states correspond, respectively, to $\pi_1^{\ddagger}$, $\sigma_{\mathrm{CBr}}^{\ddagger}$, and$\pi_2^{\ddagger}$ at the optimal geometry of the neutral target. The D_2/D_1 couplings occur after about 30 fs, and the D_0 state is populated after approximately 50 fs. Representative geometries of initial conditions, the D_2/D_1 and D_1/D_0 couplings, and the long-time limit (380 fs in practice), are shown in Fig. 3. The final conformations suggest that fragments other than Br^- may be formed. Those channels have minimal probabilities in these calculations and do not allow for meaningful statistics, but minor fragments were actually observed in the measurements. Finally, the DEA model indicates two mechanics for Br^- formation. Either the decay to the D_0 state takes place in a PES region with $\sigma_{\mathrm{CBr}}^{\ddagger}$ character and leads to fast dissociation, or the D_0 state is formed with $\pi_1^{\ddagger}$ character. In the latter case, the anion dissociates stochastically because the excess electronic energy associated with the$\pi_2^{\ddagger}$ state (~1.4 eV) is substantial.

3. Comparison of Experimental Low Energy, Differential-Angle Electron Scattering from Atomic and Molecular Targets with Theoretical Modeling

To illustrate further the interplay between the experimental results and theoretical calculations of cross-sections in collisional processes, in this section, we focus on one of the types of differential cross-sections, i.e., angle-differential cross-sections for LEE scattering. Such cross-sections often are provided for a specific electron impact excitation energy as a function of the scattering angle. Here we present a survey of recent experimental work compared to the results from theoretical models for angle-differential low energy electron scattering from isolated atoms, diatomic, and polyatomic systems in the gas phase.

3.1 Molecular hydrogen (H_2) measurements and the convergent close-coupling (CCC) method.

The electron impact excitation of the $X^1\Sigma^+_g \rightarrow b^3\Sigma^+_u$ continuum of H_2 was investigated recently, and inelastic to inelastic angle-differential cross-sections (DCSs) ratios for this system were measured accurately. In these studies, a pulsed electron beam approximately 2.5 ns wide intersected a moveable target gas beam of H_2. The scattered electrons entered a magnetic field-free and electrical field-free region of time-of-flight (TOF) 23.9 cm long and were detected by a flat microchannel electron multiplier [50,51]. A sample background-corrected TOF inelastic spectrum (elastic part of the spectrum was recorded also but is not shown) obtained is shown in Fig. 4(a). DCSs were determined for incident electron energy (E_0) values ranging from 9 to 25 eV for scattering angles that ranged from 20° to 130°. Fig. 4(b) shows an example comparison of the DCS determined for the excitation of the $b^3\Sigma^+_u$ continuum at 20 eV after normalizing counts to the elastic peak (see [51] for full details) that was normalized using elastic DCSs reported earlier [52]. The comparisons in Fig. 4(b) show improved error bars from the TOF experiment and excellent (benchmark) agreement with those calculated using the convergent-close coupling (CCC) model [51]. It is important to note that the TOF measurements do not encounter systematic errors potentially attributable to detection limits for electron transmission in other experimental methods [51]. Therefore, these improved measurements provided transmission-free calibrated DCSs for the excitation of H_2 that were normalized with quantitative elastic DCSs for the same energy loss spectra [52]. These cross-sections supplement DCSs for important transitions in H_2, e.g., the $X^1\Sigma^+_g \rightarrow b^3\Sigma^+_u$, $B^1\Sigma^+_g$, $c^3\Pi_u$, $a^3\Sigma^+_g$, $C^1\Pi_u$, and $E(F)^1\Sigma^+_g$ electronic states, measured with conventional electrostatic spectrometers, which have better energy resolution than TOF spectrometers, but have the transmission problems mentioned above because of their electrostatic focusing fields. The DCSs for other electron impact excitations of these transitions were also obtained recently and provided good, but not benchmark, agreements with the CCC method [53].

3.2 Carbon monoxide (CO) measurements and the R-matrix method for molecules.

The details of the experimental apparatus using a conventional electrostatic electron spectrometer are given in [54]. The instrument is a well-tested, low-energy double hemispherical unit with an energy resolution typically between 35 to 50 meV and scattering angles up to 130°. The gas target was introduced perpendicular to the scattering plane (defined by the spectrometer gun and detector) using a moveable thin aperture gas source [55]. This instrument has been used

extensively for several atomic and molecular targets. In the case of the electron impact excitation of CO, the DCSs reported in the past were available only for certain energy ranges. Therefore, to obtain comprehensive information over a full range of electronic states, the new study measured full electronic state DCSs [56] that were targeted to consolidate partial state DCSs [57] with those of the full-state DCSs [58,59]. Moreover, a B-spline R-matrix code was developed [60], and its results were compared to the new measurements of excitation of the $a^3\Pi$, $a'^3\Sigma^+$, and $A^1\Pi$ valence electronic states of CO. DCSs were obtained by unfolding the energy loss spectra from CO using spectroscopic data at E_0 values for the $a^3\Pi$, $a'^3\Sigma^+$, and $A^1\Pi$ valence states' excitation at energies between 6.3 to 20 eV and angles from 20° to 120° [56]. Fig. 5(a) shows a comparison of the $X^1\Sigma^+ \rightarrow a^3\Pi$ excitation at E_0 of 15 eV. This comparison showed excellent agreement between theory and most of the experimental data sets at lower energies below 15 eV. At higher energies (not shown), the agreement declines. The R-matrix models, particularly the UKRMol+ Model B, which is considered superior to the regular UKRMol and the UKRMol+ Model A because of the involvement of more states, pseudostates, and polarization, showed improved modeling of the $X^1\Sigma^+ \rightarrow a^3\Pi$ excitation [56] compared to earlier work [61] that employed SMC methods. This excitation provides test inelastic DCSs for CO as all of the low-energy experimental data [56-58] are within the error bars.

For other transitions under study, such as the dipole-allowed $X^1\Sigma^+ \rightarrow A^1\Pi$ transition, there is still the difficulty of calculating the forward scattering because of the increased partial waves at small scattering angles. However, the UKRMol+ codes provide better agreement than the UKRMol and SMC methods [61], as they include polarization terms. In fact, at $E_0 = 15$ eV, they show excellent agreement with the two more recent measurements [56, 58]. Moreover, for the weaker $X^1\Sigma^+ \rightarrow a'^3\Sigma^+$ excitation, the agreement between experiments and previous studies is very good [56,57], and the UKRMol+ Model B shows improvement over the UKRMol and UKRMol+ Model A. For this state, the partial electronic state DCSs [57,58] had to be scaled up by a factor equal to the Franck-Condon factor ratio of the full and partial spectrum (here approximately 5) to include the full spectrum excitation of this excitation [56]. More details of the CO valence state excitation is reported in [56].

Recently, this work was extended to investigate the Rydberg states of CO, i.e., the excitation of the $X^1\Sigma^+ \rightarrow b^3\Sigma^+$, $j^3\Sigma^+$, $B^1\Sigma^+$, $C^1\Sigma^+$, and $E^1\Pi$ states detailed in [62]. Here the agreement between theory and experiment for the valence states across all of the Rydberg states studied is significantly poorer than reported in previous work [56], although the experimental DCSs showed good agreement in most cases. An example of this is shown in Fig. 5(b) for the $X^1\Sigma_g^+ \rightarrow B^1\Sigma^+$ transition, in which the UKRMol models disagree over orders of magnitude. The study of the excitation of CO Rydberg states demonstrated the difficulty of modeling the excitation of these diffuse electronic states, and raised an important area for theory, particularly close-coupling models like the R-matrix, to encourage theoretical efforts to improve the models available using improved wave functions.

3.3 Krypton (Kr) and xenon (Xe) measurements and the relativistic B-spline R-matrix method

Here we focus on some examples of measurements and calculations of electron impact excitation cross-sections of rare gas (atomic) targets. In the case of krypton, the excitation of the Kr {1} $4p^6\ ^1S_0 \rightarrow 4p^5 5s[3/2]_2$, {2} $4p^6\ ^1S_0 \rightarrow 4p^5 5s[3/2]_1$, {3} $4p^6\ ^1S_0 \rightarrow 4p^5 5s'[1/2]_0$, and {4} $4p^6\ ^1S_0 \rightarrow 4p^5 5s\ '[1/2]_1$ transitions were re-measured and reported recently [63]. The particular focus of this work

was on the ratios of the scattering electron impact excitation DCSs (σ) for these excitations, which were proportional to the electron scattering intensities in the energy loss spectra. These ratios have been defined as $r = \sigma\{1\}/\sigma\{3\}$, $r' = \sigma\{2\}/\sigma\{4\}$, $r'' = \sigma\{1\}/\sigma\{2\}$, and $r'' = \sigma\{3\}/\sigma\{4\}$ (see [63] for details). The states {1} and {3} are well *LS*-coupled $^3P_2$ and $^3P_0$ states that can be only excited by spin-exchange through electron exchange, by spin-orbit coupling in the target, or via the continuum incident electron. The ratios were determined more precisely in the recent work and provided information on dynamic effects [63]. Here, only the r'' ratio is discussed for brevity, as this ratio shows the fewest uncertainties. Full discussions are given in [63], to which the reader is urged to refer. In Fig. 6(a), the experimental results [63] are compared to those from the earlier work [64] and with the relativistic (Dirac) B-spline R-matrix model (DBSR), which is the most advanced R-matrix close-coupling model available for atoms[1]. As seen in Fig. 6(a), there is an impressive agreement for r'' at 11.5 eV, but such was observed at all energy values for a rare gas target with dominant relativistic effects.

Moreover, as the smaller error bars indicate, these recent results have much-improved statistics compared to previous work. At the lowest E_0 of 11.5 eV, approximately 1 eV above the threshold, both theoretical and experimental results show very good agreement in their maxima, which were shifted from each other by an angle of 2°. At small scattering angles, the r'' values are non-zero and suggest significant non-zero spin-exchange, because the numerator of r'', i.e., $\sigma\{1\}$, depends on a spin-exchange excitation of approximately 99.6 % of the $^3P_2$ state [63]. This non-zero, small-angle spin-exchange is also observed at E_0 = 12.0 eV with excellent agreement between the experimental values [63, 64] that is observed at higher E_0 values as well. It is important to note that the near-threshold rapid change in r'' from E_0 of 11.5 eV to 12.0 eV is attributable to resonances in this energy region. On the other hand, there are still certain discrepancies between the experimental values and those obtained from the DBSR theory at angles approximately 70° to 80° for higher E_0 values. Nevertheless, the agreement between the experiment and theory is excellent overall and shows good progress in theoretical modeling. At higher E_0 values, the r'' ratio approaches zero as the scattering angle becomes smaller, showing the conventional decrease of spin-exchange.

Interestingly, in the earlier work, the non-zero spin-exchange at small angles for Ne indicated the unusual orientation of the target excited by electron impact at small angles in the excitation in which the reversal of the angular momentum perpendicular to the scattering plane was interpreted [65]. The excitation was the resonance transition of the $2p^5 3s[3/2]_1$ *LS*-coupled $^1P_1$ component, which is mixed to some extent with the *LS*-coupled $^3P_1$ component. This excitation via spin-exchange allows the perpendicular angular momentum to reverse, which is not the case in a direct singlet to singlet excitation.

The DCS ratios measurements and calculations were extended recently to another rare gas target, that is Xe [66], for which the agreement between experiments and the DBSR theory is found to be less than that for Kr. Therefore, further improvement of theoretical approaches is still necessary for electron scattering processes that involve multi-electron atomic targets as described in [66].

[1] Dr. Oleg Zatsarinny provided the results before his passing in January 2021

3.4 Chloroform ($CHCl_3$) measurements and the Schwinger multi-channel and molecular complex optical methods

This subsection presents the latest studies of elastic scattering from polyatomic molecules, aimed at biologically related molecules. Until now, cross-sections for elastic scattering from numbers of polyatomic molecules in the gaseous phase have been investigated for several decades; here, only two examples of elastic scattering from chloroform $CHCl_3$ [67] and dichloromethane CH_2Cl_2 [68] are mentioned, highlighting the recent experimental investigations compared to the results of theoretical models. Both molecules are halogenated derivatives of methane and their elastic scattering DCSs were measured using the relative flow method (RFM) with helium (He) as the standard gas. The RFM is a well-established technique, but this experiment ensured that the gas beam profiles of He and $CHCl_3$ were the same by employing a thin aperture gas target source [55]. In addition, the gas beam could be rotated in and out of the collision center, which allowed accurate backgrounds from secondary elastically scattered electrons to be determined. The electron beam value was calibrated by measuring the He- 2^2S resonance at 19.366 eV [69] to within 0.05 eV. The DCSs were obtained with two experimental setups and were overlapped at energies of 20 and 30 eV. The experimental data at low energy were compared with the results from both the SMC method with pseudopotentials in the static-exchange plus polarization approximation (SMC-SEPP) and the molecular complex optical potential (MCOP). Unlike the close-coupling models discussed in the previous sections, these theoretical approaches are perturbative and thus, applicable only over limited energy ranges. The comparison results show reasonable agreement around E_0 of 10 and 15 eV, which is observed typically for the SMC-based calculations for most targets. Above the ionization potential of $CHCl_3$, i.e., approximately 11.4 eV [70], both models are insufficient because these theories do not account for the infinite number of Rydberg states' excitation channels that open below the ionization threshold. An example of DCS values at 20 eV as a function of scattering angle obtained from experiments and calculations can be seen in Fig. 6(b). At lower energy ranges (approximately below 5eV), the disagreement between the theoretical and experimental results increases. Nevertheless, the fact that the SMC theory can model elastic electron scattering from large and complex polyatomic targets still provides valuable information; for example, it is able to model elastic electron scattering from large molecules with a mass greater than 100 amu, such as xylene [71].

4. Recent Advances in Ion Imaging Measurements of Electron-Molecule Interactions

This and the following two sections focus largely on selected experimental advances for studies of molecular dissociation initiated by LEEs. However, as in previous sections, they include certain theoretical aspects, and even in some cases, were developed to prove theoretical models and assumptions.

In this section, we present ion imaging techniques used to measure kinetic energy and angular distributions of atomic and molecular fragments that contain a wealth of information on the dynamics of dissociative electron-molecule interactions. The kinetic energy released in the dissociation of a TMA provides valuable information about the electronic states and vibrational

energy stored in molecular fragments. Further, the angular distribution is determined by the orientation of the molecule at the instant of the collision and the dynamics of the transient species before and during dissociation. For gas targets oriented randomly with respect to the electron beam, the collision process selects preferred orientations of the target molecule depending on the initial electronic state and the electronic states of the species excited by the collision. The angular distributions of fragments are highly sensitive to the coupled electronic and nuclear dynamics of the excited molecule, as it evolves to dissociation via competing pathways or nonadiabatic transitions such as conical intersections between the PES of excited electronic states [26]. A technological breakthrough to detect charged particles occurred following the development and release of microchannel plate (MCP) electron multipliers in 1971 [72]. It was not until a second crucial breakthrough occurred more than two decades later, when fast position- and time-sensitive anodes and readout electronics were developed [73], that experiments could image and mass-resolve many ions in parallel simultaneously, separated by their different flight times. Early electron-molecule collision experiments relied nearly exclusively on single-channel electron multipliers [74]. Precise measurements of energy-resolved collision cross-sections by electron or ion detection, and angle-differential cross-sections for elastic and inelastic electron scattering, as mentioned in the previous section, were achieved using energy-dispersive spectrometers to transmit and count a small fraction of the electrons selectively or ions within the specific momentum range of interest. Prominent examples of these pioneering experiments include the electron impact ionization reported earlier [75] and the DEA experiments [76] that used single-channel electron multipliers for angle-differential ion detection. These angle- and energy-differential cross-section measurements of electron-molecule collisions laid the foundation that allowed experiments[Azria, R., Y. Le Coat, and D Simon. "Dissociative Electron Attachment on H2S: Energy and Angular Distributions of H^- Ions." *Journal of Physics B: Atomic and Molecular Physics* 12, no. 4 (1979): 679. doi: 10.1088/0022-3700/12/4/016; Cadez, I, M Tronc, and R I Hall. "Dissociative Electron Attachment in CO: Angular Distribution of the O^- Ions." *Journal of Physics B: Atomic and Molecular Physics* 8, no. 5 (April 1975): L73–76. doi: 10.1088/0022-3700/8/5/003.
] to achieve higher energy and angular resolution, many of which are found in comprehensive reviews [13,77-79]. For electron impact ionization of molecules, electronic correlations and dynamics in the molecular frame were studied using complementary experimental tools developed in parallel to exploit electron-electron [80-83] and electron-ion coincidence methods [84].

Experimental measurements of highly differential electron collision cross sections benefit from the collection of a broad range angles or energies in high parallel, which can reduce the complexity of angle- or energy-scanning spectrometers, and greatly increase the data collection rate. Imaging MCP detectors allow the position- and time-sensitive detection of electrons and ions to preserve two-dimensional (2D) momentum information using the detector's active area, or three-dimensional (3D) using the detected position and the arrival time of each particle. By dispersing the electron or ion momentum in space or time, electron-molecule collision experiments can achieve energy- and angle-resolved measurements for electrons or ions subsequently, while collecting such data over a broad range of angles and energies in parallel. This parallelization makes it possible to collect more data during an experimental run, which is essential for experiments that involve many reaction channels and many degrees of freedom, or

detect two or more particles in coincidence. We review below some of the recent advances in ion imaging measurements of electron-molecule collisions. Further information on these techniques and specific examples can be found in recent general and topical reviews [13,26,85,86].

4.1 Velocity map imaging

Ion imaging systems for electron-molecule collisions are built upon the earlier developments in ion imaging detectors [87-91] to measure dissociation products from photolysis, photoionization, and bimolecular collisions in molecular beams. These early developments allowed spectrometer designs to be refined to resolve the electron or ion kinetic energy precisely by mapping all particles with the same initial momentum to the same point at the detector by velocity map imaging (VMI) [92]. Typically, imaging detectors are insensitive to the direct detection of photons with energies below the work function (approximately 4.85 eV for silicon [93]) of the front face of the detector. Therefore, many of these experiments were not subject to the significant noise background attributable to the scattered or incident radiation. On the other hand, electron-molecule collisions demand careful consideration of the incident electron trajectory in the spectrometer, because the signals desired are often obscured by a background that can arise from electrons scattered or transmitted through the gas target, or from secondary electrons or ions generated by energetic electrons hitting the surfaces in the spectrometer. Usually, this issue is addressed by collecting and trapping the transmitted electron beam effectively, using shielding to prevent undesired electrons from reaching the detector, pulsed electron beam and ion extraction fields, and/or a magnetic field parallel to the incident electron beam. It is also desirable to employ weak electric fields in the spectrometer so that fringe fields outside it have a negligible influence on the electron beam [94,95]. VMI can employ a 2D or a 3D ion imaging detector. Depending on the type of detector employed, VMI projects the 3D ion momentum distribution onto a 2D map of positions, or a 3D map of positions and time. DEA reactions have been investigated by several groups [Krishnakumar, E., Prabhudesai, V. S. & Mason, N. J., Nat. Phys. 14, 149–153 (2018). | DOI: 10.1038/NPHYS4289; Wang, Xu-Dong, Xiao-Fei Gao, Chuan-Jin Xuan, and Shan Xi Tian. “Dissociative Electron Attachment to CO2 Produces Molecular Oxygen.” *Nature Chemistry* 8, no. 3 (March 2016): 258–63. doi: 10.1038/nchem.2427; Jana, Irina, and Dhananjay Nandi. “Kinematic Study of O^- Ion Formation from Dissociative Electron Attachment to SO_2.” *Physical Review A* 97, no. 4 (April 19, 2018): 042706. doi: 10.1103/PhysRevA.97.042706.] using the time-slicing method to select a thin slice of the 3D anion fragment distribution. One alternative to time-slicing is to apply an inversion algorithm such as pBasex[G. A. Garcia, L. Nahon, and I. Powis, Review of Scientific Instruments 75, 4989 (2004). https://doi.org/10.1063/1.1807578] or polar onion peeling[G. M. Roberts, J. L. Nixon, J. Lecointre, E. Wrede, and J. R. R. Verlet, Review of Scientific Instruments 80, 053104 (2009). https://doi.org/10.1063/1.3126527] to reconstruct the 3D distribution.

4.2 Reaction microscope ion momentum imaging

Several examples of ion and electron momentum imaging of electron-molecule collisions employ the reaction microscope or cold target recoil ion momentum spectroscopy (COLTRIMS) approach [96-99]. Reaction microscopes consist typically of one or more grid electrodes to terminate the acceleration fields. It is this feature that usually distinguishes reaction microscopes from VMI spectrometers. Grid electrodes allow weak fields to be terminated precisely, which

helps separate light anions from electrons at the position- and time-sensitive ion detector. Reaction microscopes have been employed to investigate DEA reactions for molecular gases and volatile liquids having a high vapor pressure at room temperature[26], and also some molecules with lower vapor pressures, such as uracil[Kawarai, Y., Th. Weber, Y. Azuma, C. Winstead, V. McKoy, A. Belkacem, and D. S. Slaughter. "Dynamics of the Dissociating Uracil Anion Following Resonant Electron Attachment." *The Journal of Physical Chemistry Letters* 5, no. 21 (November 2014): 3854–58. https://doi.org/10.1021/jz501907d.], which was evaporated from an oven to form an effusive beam. Another approach is to form a cold target from a molecular jet involving a supersonic expansion of the target gas into vacuum through a small nozzle, followed by a skimmer [M. Fogle, D. J. Haxton, A. L. Landers, A. E. Orel, and T. N. Rescigno
Phys. Rev. A 90, 042712, https://doi.org/10.1103/PhysRevA.90.042712]. This reduces the momentum and size of the gas target to improving the momentum resolution in the directions transverse to the jet propagation direction. Reaction microscopes are also employed widely for momentum imaging of multiple particles in coincidence [99,100].

4.3 Selected studies of momentum imaging

A recent example of momentum imaging of H^- is shown in Fig. 7(a) [101]. Here the H^- fragment dissociates from the NH_2 site of the TMA of formamide (CH_3NO) formed by the attachment of 10.5 eV electrons [101,102]. The momentum image and angular distribution in Figs 7(a) and (b), respectively, are produced using a TOF gate approximately 400 ns wide, to collect all of the H^- ions while excluding most of the background attributable to scattered electrons and heavier ions. A conical selection gate on the 3D momentum distribution was also used to project a constant volume of 3D momentum space into each bin of the 2D histogram [103]. The cylindrical symmetry of the experiment was exploited by summing the momentum distributions in the positive and negative x-directions, thereby symmetrizing the data about the electron beam direction effectively (vertical in Fig. 7). The electron energy scale and cross-sections measured by a momentum imaging spectrometer are calibrated usually using one or more well-known molecules [96]. Therefore, the magnitude and direction of the momentum can be determined for each fragment, and in this case, the magnitude of the H^- momentum was found to peak sharply at approximately 24 atomic units (a.u.), which equates to 5.6 eV in translational kinetic energy. The H^- angular distribution for this channel is sharply peaked near 180° (antiparallel to the incident electron direction), with a shallow local minimum at 45° from the incident electron direction (Fig. 7(b)).

Fig. 7(c) shows the momentum of the NH_2^- fragment produced by DEA to CH_3NO at 5.3 eV. In this case, the magnitude of the anion fragment momentum is less than 20 a.u., or 250 meV in terms of the translational kinetic energy of this fragment. Given that the thermodynamic threshold energy for the simple 2-body dissociation following the C-N break is 3.6 eV, the remaining energy greater than 1 eV is distributed into vibrational excitation, rearrangement, or dissociation of the fragments. Thus, the fragment kinetic energy distribution measured offers insight into the partitioning of translational and internal energy in the dissociating fragments. The significant internal motion initiated by 5.3 eV electron attachment to CH_3NO is supported further by the NH_2^- angular distribution in Fig. 7(d), which exhibits a broad peak near 90° relative to the incident electron direction. Electron scattering calculations were employed here to determine the

electron attachment probability in the molecular frame. By averaging the attachment probability distribution computed around any chosen direction, such as the C-N bond direction and the electron beam direction as well, the laboratory-frame fragment angular distribution can be predicted within the axial recoil approximation, which assumes that the dissociation coordinate does not rotate. The black curve and the blue dot-dashed curve show the results of complex Kohn electron scattering calculations [101] that yield the angular distribution of NH_2^- for two different Feshbach resonances of A'' and A' symmetry, respectively. The green dashed curve shows the result for the A' resonance with a 30° rotation of the dissociation axis to larger O-C-N angles, which simulates the internal motion of the molecule before dissociation. The angular dependence of dissociating fragments, even if it is nearly isotropic as in the present case, provides crucial information about the dynamics of the TMA.

An existing high energy resolution electron-molecule collisions apparatus was modified recently [104] to measure kinetic energy and angular distributions of anionic fragments by velocity slice imaging. Velocity slice imaging uses the VMI method, but an appropriate electronic or software gate on the 3D momentum distribution allows the kinetic energy and angular distributions to be extracted without an inversion algorithm [92]. Using this setup, the symmetry of DEA shape resonances in planar and nonplanar chlorinated hydrocarbons was investigated, as well as the role of dynamical coupling of σ* and π* electronic states of the TMA [105]. We review two examples of these results in Fig. 8, which shows the velocity slice images and angular distributions of Cl^- fragments produced in DEA to vinyl chloride (C_2H_3Cl) in Fig.s 8(a) and (b) and allyl chloride (C_3H_5Cl) in Fig.s 8(c) and (d). Electron attachment to the planar vinyl chloride molecule at 1.3 eV forms an anion shape resonance of a'' (π*) symmetry. The electron attachment probability is expected to be the highest when perpendicular to the plane of the molecule. The antibonding orbital has a node in the molecular plane enforced by this symmetry, which prevents direct dissociation of the C-Cl σ-bond in the planar geometry. The Cl^- angular distribution measured has sharp peaks at 90° and 270° orthogonal to the incident electron direction, which suggest strongly that the dissociation proceeds very near the planar geometry, with small deviations of the dissociation axis from the molecular plane.

In contrast to vinyl chloride, the velocity slice image (Fig. 8(c)) and angular distributions (Fig. 8(d)) for DEA to the nonplanar allyl chloride molecule show that Cl^- is released in directions parallel and antiparallel to the electron beam direction. This is consistent with the fact that allyl chloride has a high probability of electron attachment to form the σ* transient anion when the molecule is oriented with the C-Cl bond parallel to the incident electron. The TMA then dissociates directly by the C-Cl break.

Many recent ion imaging advances have built upon the early and interim developments to study ionization processes upon charged particle impact [85]. Electron-impact ionization can be investigated in great detail by imaging one or more electrons and ions in coincidence using dedicated electron and ion detectors in a reaction microscope shown in Fig. 9(a) and a set of experimental conditions to ensure that the electrons and ions detected derive from the ionization of one isolated molecule or cluster [106]. This approach allows specific ionization processes to be isolated and analyzed, even if many open dissociation channels are present.

For example, dissociative double ionization upon an electron collision with a molecule leads to two ionic fragments that can be detected in coincidence together with one, two, or three electrons. This approach was used recently to isolate (Fig. 9(b)) and study the dynamics of intermolecular Coulombic decay (ICD) in the water-tetrahydrofuran (THF) dimer [100], which is a simple model of a hydrated biomolecule. ICD is an ultrafast intermolecular electronic process that allows the nonradiative relaxation of an excited molecule in an environment by transferring energy to a neighboring molecule. In this study, electron impact ionization causes an inner-valance electron to be emitted from the water molecule in the dimer, after which a valence electron from the water molecule fills the inner-valence vacancy and transfers the energy difference to the neighboring THF molecule, from which a low-energy ICD electron is emitted [100]. The resulting water and THF cations dissociate in a Coulomb explosion, and the THF cation may undergo subsequent dissociation processes such as hydrogen loss. This process was identified by comparing the kinetic energy spectrum of electrons detected in coincidence with H_2O^+ and either $C_4H_8O^+$ or $C_4H_7O^+$ ions with the spectrum of inner-valence ionization of water monomers. The analysis revealed an enhancement in the yield of LEEs that is a clear signature of ICD.

5. Importance of Neutral Detection in Electron Scattering Processes

In addition to information about the dynamics of dissociative electron-molecule interactions presented in the previous section, identification of the products that result from electron impact dissociation of molecular targets in their gas phase and determination of their cross-sections have always been fundamentally important to describe the nature of the scattering process. Further, knowledge of these species' production can be used in computational modeling of related processes for various applications, including radiation, cluster, and plasma sciences. Since the invention of mass spectrometry [107], this technique has provided a detailed description of the formation of the dissociation products, their yields, and appearance energies [108]. Most of the experimental effort has been focused on measuring cations and anions because of the relative ease of detecting charged species in a mass spectrometer. However, electron collision-induced dissociation can lead to one or more neutral fragments of the target molecule. The fragments that are formed may contain at least one unpaired electron in their structure, so they are referred to as free radicals. Because radicals are more reactive than the target molecule usually, they can lead to other secondary processes upon interaction with adjacent molecules. However, it has been particularly challenging to identify them because of technical limitations in detecting neutral products, particularly those in their electronic ground state. In the past, several different methods have been used to overcome this drawback. Here, we will focus on one of these methods in which mass spectrometry is used to probe the neutral products formed when electrons strike molecular targets. This method was used recently to detect neutral products attributable to the DEA process [109]. Therefore, we review some of the historical developments in neutral detection briefly, and focus primarily on a mass spectrometric technique based on which the initial results from DEA to CCl_4 were observed. However, other methods that aid in neutral dissociation have been developed, and are mentioned also.

5.1 Initial efforts in detection of neutral dissociation products

Experimental detection of neutral products, such as excited species or free radicals, is challenging because they cannot be accelerated in electrostatic fields above the detection threshold energy required by many types of detectors and they may have finite metastable lifetimes shorter than their time of flight in an experiment. In addition, in the case of radicals that are often produced in their ground electronic state, their detection presents a challenge because they are highly reactive as well. Even so, the first attempts to detect radicals by mass spectrometry were reported in the early 1950s [110]; however, other methods had been used already several decades before to detect the ground-state neutrals formed from molecular dissociation [111].

In the early mass spectrometric works, free radicals from a series of molecular targets were detected usually as products of several reactions, such as heterogeneous and homogenous thermal decomposition, combustion, electrical discharges, and reactions with excited ions. To detect them, a molecular beam that contained different products of the reaction under study was introduced into the ionization region of a mass spectrometer and subjected to electron collision. To distinguish the radicals formed in the initial reaction from those of the same molecular weight that resulted from the electron dissociation of other reaction products, two methods were used in a mass spectrometer [110]. The first was based on the fact that the ionization energy of the free radical is lower than the energy needed to produce the same radical from the molecular target, i.e., the so-called "appearance energy". Thus, more energy is required to dissociate and ionize the molecular target to form the radical than simply to ionize the radical. The difference in energy for both corresponds to the bond dissociation energy, which typically is approximately 3 - 4 eV. Therefore, using an energy above the ionization energies of the free radicals, but lower than its appearance energy, will allow detecting the radicals from the initial reaction. The nature of radicals based on their molecular weight and ionization potential was deduced previously for a series of hydrocarbons [111,112]. In these experiments, the molecular target was subjected to a 200 eV electron impact, and the fragmented neutrals were identified by varying the electron energy of the second electron beam, which could be continuous or pulsed [113].

In the second method, higher energies were used, i.e., in the range of 50 – 200 eV, which corresponds to the energies with the maximum cross-section for ionization of gas-phase targets. The ion yield for the free radical formed in the initial reaction was compared to the yield that originated from the electron impact dissociation of the molecular target without the initial reaction applied, so the mass spectrometer acted as a standard residual gas analyzer. Both yields were subtracted from each other, and the resulting value was attributed to the signal from the free radicals the initial reaction produced. Because the branching ratio of the products from the molecule can change slightly from one experiment to another, this method was unsuitable for low concentrations (less than several percent) of radicals. However, it was used extensively to detect radicals as their ionization cross-section was much higher than in the first method. As mentioned previously, this method was used primarily to detect the radicals from specific reactions, while the first attempts were used to detect neutral products of the electron impact scattering for the molecular target, such as ammonia [114] and water [115].

In one of these early studies, the total and partial cross-sections were measured for all ionic and neutral products that originated from water vapor at the electron impact of 100 eV. The detection of free radicals was achieved using the dual-beam and high transmission ion sources in a mass spectrometer (Fig. 10(a)). The basic principle of such an experimental arrangement with two

filaments was to produce neutral or unstable species in the first ion source and ionize them subsequently in the second ion source. The distance between two electron beams emitted from the filaments was approximately 2.5 mm to reduce the transition time of products from one source to another. A molecular target was introduced through the inlet and entered into the first ion source in which specific products were produced by adjusting the energy of the electron beam. For example, with energies below the target's ionization energy, free radicals, anions, or excited species were formed. The products formed there diffused through a slit that had a diameter of a few microns into the second ion source where they were ionized by sufficiently high energy to be detected by the mass spectrometer. Optionally, by applying potential with different polarities to the ion repeller in the first ion source, anions or cations were allowed to pass to the second source. Such a set-up was tested primarily to detect the excited states, i.e., the 1s2s level of He [116], and later, it was used for other molecular targets. For example, in the case of the dissociation of water induced by 100 eV electrons, it was estimated that the majority of the products consisted of cations, and nearly one-third were neutrals, and the abundance of anions was approximately three orders of magnitude lower than that of the other species [115]. While in the case of the dissociation of ammonia, approximately 40% of the products of the electron impact consisted of neutrals. Later, a similar dual-chamber approach was used to study the mass spectrometry of neutral formation from the electron impact of aromatic compounds [117] and other simple hydrocarbons [118-120], as well as more complex compounds such as tetramethyl derivatives [121].

The plasma community has been using this methodology largely to measure cross-sections and detect radicals derived from electron impact in the gas-phase of halogenated compounds such as methane (CH_4) [122,123]; carbon tetrafluoride (CF_4) [124]; silicon tetrafluoride (SiF_4) [125]; trifluoromethane (CHF_3) [126], and sulfur hexafluoride (SF_6) [127,128]. In these plasma studies, this methodology is known as "appearance mass spectrometry" because it is based on measurements of the appearance energy of the radicals formed from the target's dissociation, which is compared to the ionization energy of the same radical [129]. Further, it is still used in the diagnostics of neutral species in plasmas [130]. Surprisingly, most of these studies identified neutrals from the electron impact processes that occurred at higher energies. Only some reports mentioned the possibility of using the electron beam at energies as low as 6 eV, where the energies in neutral dissociation and the DEA process can occur, in the first ion source to produce free radicals, anions, or excited species [116].

5.2 Neutral detection from DEA to carbon tetrachloride (CCl_4)

As mentioned above, the possibility of neutral detection at low energies was stated in an early work, but no experimental data were provided [116]. As a result, no studies on neutral detection from the gas-phase DEA process were reported until 2017, when a method similar to that described in a previous subsection was used to detect neutral products from DEA to carbon tetrachloride (CCl_4) near 0 eV electron impact [109]. However, it is important to mention that a study was conducted approximately four decades ago in which the detection of radicals from this low-energy process was attempted. In this study, radical fragments were measured indirectly from the low-energy (<0.5 eV) electron impact on CCl_4, $CFCl_3$, and $C_2F_2Cl_2$ by using a hot filament as an electron source and the off-line method was used to detect products that were collected after the experiment [121]. Radicals produced from these compounds were determined

based on potential radical-molecule reactions or reactions among all products, and on reaction enthalpies, which were calculated using the heats of formation of the various species. For example, in the case of CCl_4, it has been deduced that the CCl_3 radical and neutral species of CCl_2 are the most abundant products formed by electron attachment to the target molecule [121]. In contrast, a more recent study, which probed the potential fragments that resulted from gas-phase DEA to CCl_4 near 0 eV, reported only the formation of CCl_3 radicals [109].

In this recent study, only one filament was used rather than two ion sources with two filaments, as was used in the previous double chamber studies; instead, two steps with specific parameters of the ion source were iterated over many cycles (Fig.s 10(b) and (c)). Further, after their ionization, the radicals were analyzed by a mass spectrometer, as was the case earlier. The electron beam that was formed was pulsed, and had alternating energies that corresponded to the energy of the DEA process in the first step and to the energy that is sufficient to ionize the radicals that are formed in the next step. Then, the signal at the specific mass to the charge ratio or the entire mass spectrum was recorded by a quadrupole mass spectrometer. Next, these two steps, in which the electron energy and the length of pulses could be set for each step, were repeated over many cycles, and the signal was integrated.

Two types of experiments were performed in this recent study. In one, the electron energy in the first step was increased in each cycle over the electron range between 0 and 3 eV, while the energy in the second step was constant at 11 eV throughout the experiment (Fig. 10(c)). In the second experiment, the electron beam was scanned over the energy range at which the DEA process is expected, and, in the second step, the electron energy was scanned in a wide range to determine the energies at which the radicals produced from the DEA were detectable. In the first step, the signal was integrated over a range of energies because choosing one energy, e.g., 0.5 eV, resulted in a small number of counts that would require a relatively long time to acquire. The drawbacks of a long acquisition time are that it is time-consuming, and the electron beam and other electronic parts of the ion source can become unstable.

Fig. 11 shows the electron impact yield of CCl_3, in which the signal from the first step was collected over the energy range from 0 to 3 eV, and the energy of the second step was scanned between 6 and 11 eV. The ionization energy of CCl_3 was determined to be 8.5 eV, which was in good agreement with the results of previous studies. In addition, the fig. presents the yield of CCl_3^+ formed by the electron impact dissociation of neutral CCl_4 measured by the conventional method without the first step to induce DEA. Further, the lifetime of the CCl_3 radical was estimated in this study, and other products that can originate from CCl_3 fragmentation were identified by comparing their appearance and ionization energies. However, in this study and any other studies in which a hot filament has been used for ionization, it is very important to consider that thermal dissociation of the target molecule can occur close to or at the filament [131]. To avoid such thermal effects, other ionization techniques can be used to detect radicals, as has been shown for desorbed species produced in DEA to the molecular targets in the condensed phase, in which photons were used to ionize the products [132,133].

5.3 Neutral detection by other techniques

Experimental methods, other than the above two ionization methods by electrons and photons, can be used to determine radicals from the processes caused by the electron impact. One such

method uses specialized detectors based on rare gas matrices that can detect certain metastable species selectively [134]. However, there are only a few reports in which this type of detector was used. For example, in one recent study, such detectors were used to investigate metastable fragments, i.e., $O(^1S)$ and $CO(a^3\Pi)$, formed through to the dissociative excitation of methanol in the electron energy range from their appearance energy to 100 eV [135].

In another method, vacuum ultra-violet (VUV) emissions from the excited neutral products were registered to obtain atomic spectra, thus providing information about the dissociation of chemical bonds attributable to electron collisions. Recently, this method was used to investigate photon emissions from the fragments of two biomolecules, i.e., thymine [136] and adenine [137], that collided with electrons over a wide energy range, in which an excited hydrogen atom was released, so-called H loss. Although no signal corresponding to the DEA process was observed, which is expected in the case of H loss from each biomolecule [138,139], a weak, broad feature was observed at 5 eV in the adenine study [137]. As discussed in that work, the appearance of this feature may be associated with a neutral dissociation process in adenine.

In contrast to atomic fragments, fluorescence emission by molecular fragments is rare in the VUV photon region; therefore, other techniques could be used for this purpose, such as Fourier transform infrared spectroscopy or laser-induced fluorescence (LIF). It is important to note that the latter has been used previously to detect the ground state $OH(X^2\Pi)$ following electron impact on a water molecule over an energy range from threshold to 300 eV [140]. Interestingly, this study attempted to determine the contribution of OH radicals produced from DEA by deconvoluting the excitation function for OH(X) near the threshold. Therefore, it is still of great importance to adopt or develop novel techniques for neutral detection to provide new and more precise measurements of the fragments that originate from the DEA process to understand electron impact processes on molecules better.

6. Experiments with Clusters: Unraveling solvation effects upon electron attachment

This section extends technical aspects of electron scattering on isolated targets and approaches conditions in which environmental effects must be taken into account. To do so, LEE studies with clusters are necessary. From the perspective of microphysics, clusters are aggregates of atoms or molecules that range from several individual atoms or molecules to aggregates large enough to be referred as bulk matter [141]. This borderline between isolated atoms or molecules and bulk matter makes clusters of great interest in chemistry and physics because the properties (i.e., melting point, ionization energy, etc.) may change from that of an isolated species to bulk matter when simply transitioning from one size to the next [142]. Because clusters can be formed from any atom or molecule, different classes of clusters can be defined. One common classification is based on binding energy of the cluster constituents [143]. The weakest bonds found in clusters are those for rare gases; e.g., helium droplets have a bond energy of only 0.6 meV formed by weak induced dipole interactions [144]. A stronger bond (but still considerably lower than the typical chemical bond) is found for hydrogen-bonded clusters, which show a typical bond energy of several hundred meV. The clusters discussed in this section are hydrogen-bonded, which is an important aspect of electron collision studies. In the electron attachment

process, an incoming low-energy electron with a typical kinetic energy of up to several eV attaches to a target, i.e., the energy released in the target system (comprised of this initial kinetic energy and the electron affinity of the target) remains on the order of molecular bond energy and leads to dissociation [145,146]. However, in a cluster environment, a considerable amount of energy can be removed by the evaporation of the cluster constituents before the molecular bonds cleave.

A well-established experimental method to generate molecular clusters is based on the supersonic expansion technique [147]. This method uses the expansion of pressurized gas through a small nozzle orifice into a high vacuum. The gas is cooled during this expansion, which allows clusters to form when this intrinsic cooling mechanism leads to a local temperature at the level of binding energies of the clusters. Because the local speed of sound depends on the square root of the temperature, the expansion becomes supersonic. Nucleation leads to the release of condensation heat, which is compensated for by evaporative cooling of the cluster by evaporation of weakly-bonded cluster constituents. Before the cluster beam can be crossed with an electron beam, it must pass a skimmer to avoid interference of clusters with shock waves present at the edges of the expansion [148]. For a typical cluster expansion used to generate a molecular target clustered with several water molecules, a vapor of the target molecule and water vapor are co-expanded within excess of a seeding gas, which is a rare gas typically. Then, the mean cluster size can be controlled in practice by varying the pressure of the seeding gas. As the general law for the mean cluster size describes [149], two other ways to vary the mean cluster size are to lower the gas temperature before the expansion, which is impossible for gases that condense easily, such as H_2O, or change the nozzle size. However, the latter is experimentally rather laborious because the experiments are run under high vacuum.

In electron attachment experiments, the skimmed cluster beam is crossed with an electron beam of variable energy. Anions formed are analyzed subsequently by a mass spectrometer, as discussed in the previous subsection. Fig. 12 shows a schematic of the experimental setup that was used to study electron attachment to hydrated pyrimidine clusters [150]. This cluster source was built using a relatively simple construction kit that included gas valves, tubes, and tube fittings. This design allows the assembly to be adapted easily and is beneficial for samples with different vapor pressures [151]. After it passes the skimmer, the target beam is crossed with an electron beam formed by a heated filament. The product anions formed are then extracted from the ion source by an electric field and focused on the entrance of the mass analyzer. In Fig. 12, the scheme of a double- focusing mass spectrometer in reversed Nier Johnson geometry is shown, in which the momentum of anions is analyzed first by a magnetic sector field, followed by an electric sector field that acts as an energy analyzer. To detect the anions, a channeltron-type secondary electron multiplier is used. Such typical crossed beam arrangements for electron attachment studies with molecular clusters were used extensively in the 1980s and 1990s to study the formation of anions from simple molecules such as H_2O and O_2, as well as small halogenated compounds (see review [152]). Such cluster studies continued at the beginning of this century; however, in these studies, extended experimental techniques were used as well, such as using

photoelectron sources to generate LEEs with very high energy resolution [153,154], or embedding target molecules in helium droplets and studying processes at 0.37 K [155,156].

Further, in this context, previous pioneering experiments with clusters of biological relevance that used transfer reactions of bound (Rydberg) electrons should be mentioned [157,158]. Compared to free-electron attachment, Rydberg electron transfer offers post-stabilization of the TMA by the transfer agent. Therefore, even a very weakly-bonded electron that is captured far outside the molecular frame by sufficiently large dipolar forces can be detected. This has allowed relevant conclusions to be drawn for the situation, in which a free electron is captured as well. In recent years, the study of electron attachment processes in micro-hydrated clusters has received further attention [159-162], as clusters can be viewed as a basic model system of radiation damage of biologically relevant molecules in the condensed phase [100,106]. The latest results for two nitroimidazole-based radiosensitizers in the gas phase and embedded in clusters, so-called micro-hydration, are presented here.

6.1 Electron attachment to gas-phase and clusters containing nitroimidazolic molecules

Surveying the potential action of many radiosensitizers showed that nitroimidazole compounds were among the proposed potential candidates because the enzymatic reduction that involves electron transfer activates them [163]. Recently, the attachment of low-energy electrons to two gas-phase nitroimidazolic compounds, nimorazole ($C_9H_{14}N_4O_3$, referred to hereafter as NIMO) and misonidazole ($C_7H_{11}N_3O_4$, referred to hereafter as MISO), was investigated with experimental crossed-beam experiments combined with quantum chemical calculations [159,160]. These electron attachment studies were intended to determine the fundamental molecular properties in electron reduction reactions on the molecular level. The results showed that both compounds, NIMO [159,164] and MISO [165], formed an undissociated molecular radical anion that is detectable on typical timescales of mass spectrometric detection in the range of several microseconds. Based on the calculations, the formation of the molecular anion compromises electrons with energy near 0 eV, as expected because the excess energy in the TMA is too high at higher electron energies. However, near 0 eV, the electron affinity and the small surplus from the kinetic energy of the electron released can be accommodated in the vibrational degrees of freedom within the molecule (84 vibrational degrees of freedom for NIMO and 69 for MISO). Interestingly, the difference between both compounds is the availability of dissociation channels near 0 eV. In the case of NIMO, the intensity of DEA signals is relatively weak at such a low energy, indicating considerable energetic barriers or vibrational excitation of the neutral. Thus, autodetachment is the only effective competitive channel to prevent stabilizing the TMA. In contrast, in the case of MISO, several DEA channels at low energies were detected. The most abundant three anions formed upon DEA were NO_2^-, the anionic fragment, in which MISO lost CH_2 and NO_2, and OH^-. Therefore, it was proposed that the latter two are formed via molecular rearrangement. For NIMO, NO_2^- was the major fragment anion as well, which is a common fragment anion in DEA to nitroimidazoles [166,167]. However, the NO_2^- anion was formed with the highest yield at approximately 3 eV and with a relatively small yield at approximately 1.5 eV. To determine the mechanisms responsible for this fragmentation, the TMA states (shape resonances) were calculated and the cleavage of the C–NO_2 bond upon DEA in a two-step process was proposed [168]. In the first step, electron attachment to the π^* orbital

induces vibrational relaxation and thereby the population of the corresponding dissociative σ* resonance through the π*/σ* vibronic coupling mechanism [168,169]. This model is fully applicable to explain the formation of NO_2^- at both energies (~1.5 and ~ 3eV) for NIMO and MISO. Near 0 eV, a similar mechanism may be applied; however, the DEA channel is energetically possible only for MISO, while for NIMO, the single bond cleavage is an endothermic process with a threshold of +0.53 eV [159,160].

Thereafter, the gas-phase results above were compared to those for micro-hydrated radiosensitizers. As expected, the undissociated parent radical anion remained the abundant product anion in cluster experiments because the molecular cluster environment can serve as a heat sink. Moreover, the mass spectra showed the parent radical anion of NIMO and MISO with several water molecules attached [159,160]. Following semi-empirical laws for the resulting mean size of the cluster distribution, the mean number of water molecules attached increased as the pressure of the seeding gas increased [159]. The calculations performed on structures for the anionic NIMO hydrated by water showed that the anion becomes increasingly stable as the number of water molecules attached to it increases [159]. Despite different conformers considered, the trends in the energetics overall were always the same. This is because the electron affinities of NIMO hydrated by one water molecule increased in energy to the range of 1.36 - 1.76 eV, while for NIMO hydrated by two water molecules, it increased to the range of 1.53 – 1.96 eV [159]. By comparison, the electron affinity of the isolated molecules was calculated to be of 1.31 eV [170]. In addition, the calculations showed that the vertical detachment energy (VDE) of the NIMO anion also increased as the number of water molecules increased. Specifically, adding one water molecule increased the VDE to 1.83 – 2.32 eV, and the presence of two water molecules increased the VDE to 2.11 – 2.64 eV, while for the bare NIMO anion, the VDE was calculated to be of 1.68 eV [159].

With respect to the fragmentation channels upon electron attachment to NIMO and MISO, a drastic quenching of the NO_2^- anion yield was observed upon micro-hydration. The ratio of the NO_2^-/parent cluster anion yield for NIMO as a function of the cluster mean size is shown in Fig. 13 and for MISO is shown in Fig. 14(a). Both dependencies are quite similar, and the ratio shows a decrease by 1-2 orders of magnitude already by micro-hydration with three water molecules. This effect may be attributable to insufficient energy provided to the molecule for it to dissociate. Potential mechanisms of the anion stabilization may include the caging of the released NO_2^- fragment anion and/or ultrafast quenching of excitation in the radiosensitizer's TMA. In mixed cluster anions that contain NIMO and water, it can be expected that the excess charge is localized at the NIMO compound because of the significantly higher electron affinities compared to small water clusters [171]. Further, the yield ratio of the two products, i.e., NO_2^- and OH^-, and the undissociated cluster anion showed different trends (Fig. 14(a)). The trend for the fragment with OH^- is relatively constant with respect to the number of water molecules in the parent cluster, indicating independence of the hydration stage and that quenching DEA channels in this reaction is not applicable. In contrast, a decreasing trend was reported for NO_2^-, indicating that this DEA channel is diminished by hydration greatly. The calculations of both reaction energetics provided a hint about the unusual behavior observed in the experiment. The corresponding theoretical results are shown in Fig. 14(b). While the DEA process that produces OH^- is nearly thermoneutral for the neutral molecule, it becomes more exothermic as the number

of water molecules in the clusters increases. This effect has its origin in the energy gain attributable to hydration of the hydroxyl anion and can be expected to be universal because it is independent of the precursor TMA from which OH^- is released [160].

Considering the general physical phenomena of electron attachment processes in such systems, the de Broglie wavelength of the incident LEE is large, e.g., for approximately 3 eV electrons, it amounts to 0.7 nm. Therefore, even in a large water matrix with an embedded target molecule, the probability that electron attachment will occur at the target site, if the target is a so-called electron-affine compound, is highly feasible. Further, compared to the water molecule, which has a relatively low cross-section for (dissociative) electron attachment [172], nitroimidazole-based molecules exhibit larger cross-sections, and thus, represent ideal targets for electron reduction under solvated conditions.

7. Conclusions and outlook

Research on electron scattering processes is a well-established field that has witnessed several significant scientific breakthroughs since JJ Thompson discovered the electron in 1897. These discoveries transformed the frontier of physics and still have a major influence on the fundamental and applied sciences. Because there is already an enormous amount of scientific literature on this type of study, in this colloquium paper, we provided the current status of experimental and theoretical knowledge related to the field of gas-phase electron scattering only for the selected topics that lie within the authors' expertise, but are based on collaborative research with several international laboratories. However, the selection of these topics was also chosen purposely to present a handful number of examples of recent frontline experimental and theoretical studies that still have open questions or need to be improved and developed further.

In summary, the developments in theoretical methods for electron scattering have been accompanied inseparably by progress in experimental work, and their close interplay is essential for any further improved understanding and description of electron-induced processes. Because of the atomic and molecular physics community's increased interest in DEA and the usefulness of these processes in related research areas and applications, we focused on the recent development of theoretical modeling and presented its current status and challenges as well. As stated above, adapting contemporary MxQC techniques to DEA problems is an important advance, as it permits simulations to be performed in full dimensionality. As outlined in this colloquium paper, the first applications addressed systems with 12 (iodoethene), 18 (chloroethane), and 30 (5BrU) vibrational modes, in addition to the considerable number of electrons and even of anion states, at least for 5BrU. The dimensionality of the complex PESs is a major bottleneck for DEA models, and the approaches proposed, based on the FSSH and AIMS methods make the numerical effort comparable to those of photochemical problems. As can be anticipated, the breakthrough in dimensionality comes with a price. Using QC techniques to approximate the real part of the complex PES is essential for performance, but it carries some limitations. The MxQC dynamics cannot account for non-local dynamics, and considering broad resonances would be difficult even in local approximation. The occurrence of pseudo-continuum states in the QC calculations must be avoided as well, which hinders the use of diffuse basis sets

and hence the inclusion of DBSs in the active space. Finally, more complex reaction pathways and branching ratios could make modeling the local width as a function of the resonance position a challenging task.

Nevertheless, some of these limitations would plague any DEA model. The highly accurate methods are somewhat limited to the number of vibrational modes and anionic states, as they are challenged by many-mode reactions. One of the primary motivations to extend the MxQC techniques to DEA problems was the biological effects of electron-induced processes. Since the seminal work on LEE-induced DNA damage [173], a considerably large amount of DEA data have been obtained for isolated biomolecules, clusters, and even condensed systems, and theory has barely touched upon most of those data, as far as DEA simulations are concerned. Despite the difficulties in calculating accurate cross-sections magnitudes outlined above, the MxQC DEA simulations described the energy dependence of the experimental cross-sections for polyatomic systems consistently. To that extent, they can be viewed as an essential step to bridge the gap between theory and experiment.

To explore this bridge further, we surveyed the experimental progress made in the past several years that provides measurements of cross-sections, largely DCS and DCS ratios, to test electron scattering from a range of targets modeled by several frontline theoretical calculations in atoms and molecules. The survey showed areas where the models essentially represent the electron scattering process accurately and those where much progress is needed, for complex multi-electron targets, e.g. Kr, or targets with complicated open-shell structures, e.g., CO.
It is essential to investigate other targets, including atomic and molecular targets, for both elastic and inelastic electron scattering DCSs to maintain this experimental effort to test theory. Specifically, for atomic targets, re-measurements of the DCSs for Kr and Xe excitations from the ground state np^6 to the np^5 n+1p excitations are suggested, which would allow new benchmark results to be compared with the DBSR theory and earlier work [64,174]. For diatomic molecules, doubly-differential cross-sections of ionized H_2 would be a good example to test the CCC methods, as was performed for He [175]. There is also a paucity of data for elastic and inelastic scattering from O_2, NO, NO_2, N_2O, and CO_2. In particular, vibrational excitations of CO_2, the prominent greenhouse gas, would be important from the applied perspective of electron scattering processes in atmospheric physics. Further, such studies need to be extended to polyatomic targets of interest in elastic scattering, such as carboxylic acids, including formic, acetic, propionic, and butyric acids, to examine the COOH radical. Moreover, several studies on polyatomic targets require further work in elastic and inelastic scattering to standardize the inelastic DCSs measured previously, e.g., studies of a polyatomic with a resolvable inelastic structure, such as benzene, ethylene [176-178], or H_2O [179]. A broader, but important, perspective would be to measure DCSs for other molecular systems such as atmospheric and interstellar molecular constituents as well as biomolecules. Studies of electron collisions with such complex targets have shown considerable progress, but still, limited information is available. Therefore, in this colloquium paper, we stressed the importance of advancing instrumentation to explore electron scattering phenomena further. In recent years, the atomic and molecular physics community has witnessed several developments and improvements in instrumentation. However, not only because of the limit in the scope of this paper but also because of the growing interest in the dissociative processes in other research areas, we selected

examples of techniques related to the study of molecular fragmentation. The dissociative processes have been addressed in many earlier studies that provided extensive data on the fragments produced. However, they have not provided much information about cross-sections, largely because uncertainties in the signal collection, detection sensitivity, and anisotropy in the angular distribution of fragments, to mention a few [130]. Nonetheless, the rapid development of sophisticated techniques promises to overcome these technical obstacles in future electron scattering studies.

We reviewed some recent examples of ion imaging experiments used to reveal electronic and nuclear dynamics in TMAs initiated by electron collisions. The examples included DEA involving core-excited Feshbach resonances and momentum imaging of H^- fragments above the abundant scattered electron background. Moreover, velocity slice imaging experiments revealed shape resonances with σ^* and π^* symmetry in chlorohydrocarbons, with a coupling of a π^* shape resonance to a dissociation coordinate nearly in the molecule's plane. Electron-ion coincidence momentum imaging has revealed another example of electron-impact ionization involving ICD to isolate the ICD process from other ionization processes using ion momentum conservation and the kinetic energy of electrons emitted and measured in coincidence with the two cationic fragments. Recent and emerging developments in detector technologies will continue to improve the flexibility and variety of ion imaging experiments, such as higher momentum resolution and detection rates. One particularly promising direction is the development of high spatial and temporal precision camera technologies [180] that could simplify acquiring and processing ion imaging experimental data significantly. As ion imaging experiments gain increasing access to rich information on electron collisions with more complex molecules and clusters, it will be possible to test increasingly sophisticated electronic structure and electron scattering calculations thoroughly. The combination of ion imaging measurements and theory on electron-molecule interactions continues to offer rich and detailed insight into the electronic and nuclear motion in these systems.

Another significant instrumentation development was the use of mass spectrometric methods for neutral detection from the DEA process. Indeed, despite several earlier studies that have reported different methodologies to investigate neutral products formed from electron impact dissociation, most were dedicated to processes that occurred above the threshold energies for ionization. We presented the first successful trial of CCl_3 detection from DEA to CCl_4 at electron impact near 0 eV. However, there is still an urgent need to develop new complementary techniques that can be adapted for in-situ studies to detect neutral products from molecular fragmentation induced by LEEs.

Cluster techniques have been used more commonly to extend beyond the electron scattering from isolated targets to obtain insight about potential processes induced by LEEs when the target molecule is present in a more complex environment. Because clusters, similar to a molecular beam, are produced under vacuum conditions, standard mass spectrometric techniques allow the charged fragments to be detected. Thus, valuable fundamental knowledge of anion formation via DEA in a solvation stage can be gained. As shown already in the case of micro-hydrated radiosensitizers, cluster studies with the well-known halogenated nucleobases, 5- bromo- and fluorouracil, were performed earlier [181]. Meanwhile, several other potential modifications of nucleobases were proposed and investigated to improve radiotherapeutic applications from the molecular perspective [182-185]. In these studies, the established technique in which supersonic

expansion of a gas target is applied, has been a suitable way to generate neutral target clusters for the electron attachment process. For future electron attachment studies with clusters, it may be desirable to select neutral clusters with a specific size before the interaction with an electron. The experimental results could be compared unambiguously with theoretical calculations in such a case as well. Thus far, varying expansion conditions during experiments have led to different mean cluster sizes overall and have provided a rough assignment of neutral precursor ion yields observed, although this method is still indirect. To overcome this challenge and be able to select the target cluster size, using another experimental concept that was attempted in recent years to achieve a specific selection of neutral clusters before their collision with photons is proposed. In this case, the size selection is based on the Stark deflection technique, which exploits the different dipole moment of clusters with a different size, and leads to slight spatial displacement of clusters with a specific size after passing the inhomogeneous electric field zone [186]. For example, such spatial separation was observed for pyrrole and pyrrole-water clusters [186]. Recently, the selection of small ammonia clusters doped with sodium was also achieved by magnetic deflection [187]. However, no application of this technique has been realized thus far to study electron attachment processes, which often possess a considerably low cross-section. In addition, the well-known electro-spray ionization (ESI) technique [188] could be used to generate specific cluster targets for DEA. ESI is applied to transfer large biomolecules into the gas phase, and some collision studies with ESI-generated micro-hydrated systems have been carried out previously [189-191]. The production of charged clusters allows a specific target size to be separated by standard mass spectrometry. However, dedicated electron attachment studies, e.g., those that measure the fragmentation yield as a function of the electron energy using a well-defined electron beam, have not been performed with clusters to date, although electron-induced dissociation has been conducted under the more common expression of electron capture dissociation, which is a standard method used in ESI-mass spectrometry largely in peptide and protein research [192].

Finally, this shift in study direction toward electron-cluster target interactions involving more complex heterogeneous systems relevant to either biological or dense astrophysical plasma that cannot be replicated by standard gas or even condensed phase conditions has been observed in the atomic and molecular physics community in recent years. Therefore, more attention has been given recently to other possible electron-induced processes attributable to the presence of the environment, such as ICD, which was mentioned already. Moreover, another environment-assisted process related to DEA, because it involves a capture of a free electron in an unoccupied orbital, is interatomic Coulombic electron capture (ICEC). This is an alternative mechanism of energy relaxation in a weakly bound system in which, after an electron is captured in an atom or molecule's unoccupied orbital, energy is transferred to a neighbor that becomes ionized [193-195]. Theoretical predictions have shown that depending upon the distance from the neighbor, the ICEC cross-section can be up to several orders of magnitude higher than the radiative electron capture cross-section, which is a competitive process in an atomic system. Moreover, it was found that the ICEC cross-section becomes maximal when the incoming electron has kinetic energy near 0 eV [193]. Previously, the theoretical ICEC cross-sections for some prototype systems were compared to the radiative electron capture cross-sections [193,194]. The systems investigated were, e.g., Ne^+ with Xe or benzene, and He^+ with Ar or benzene as neighbor species, respectively [193], and very recently, a proton in the vicinity of a water molecule [196]. Other

ICEC systems studied were Mg^+ with Br^- as a neighbor and Mg^{2+} with several water molecules as neighbors [194]. In these cases, it was found that the ICEC cross-sections tend to increase linearly with the number of surrounding water molecules, indicating the importance of ICEC as an environmental process. Unfortunately, although a vast number of ICEC systems has been studied theoretically, no experiment has confirmed the predicted ICEC process successfully thus far and accordingly, it is awaited eagerly [197].

Because of the length constraints, this colloquium paper simply scratched the surface of recent experimental and theoretical efforts in the atomic and molecular physics community, and was limited to only several important topics. We have presented specific challenges and needs in electron scattering by presenting concrete examples of studies that can pave the way for further scientific advancements and new research opportunities. Therefore, we believe that this colloquium paper is informative and will stimulate research activities for new scholars in the field as well as readers in other related fields.

Acknowledgments

SP is supported by the US Department of Energy Office of Science, Office of Basic Energy Sciences under Award Number DE- FC02-04ER15533 (NDRL No: 5359).

MTNV acknowledges support from Brazilian National Council for Scientific and Technological Development (CNPq), grant 304571/2018-0, and also thanks Dr. Fabris Kossoski and Dr. Lucas M. Cornetta from comments and suggestions about the theoretical methods part.

MAK gratefully acknowledges funding by the US National Science Foundation under Grants No. NSF-RUI AMO 1606905 (supplement 1303071) and 1911702, which provided funds for his postdocs (Dr. A. Sakaamini and earlier, Dr. L. R. Hargreaves), undergraduate students and for undergraduate and Masters' students to travel to Brazil to do research. Several postdocs (e.g. Drs. M. Zawadzki, K. Fedus) were partially funded through the International Fulbright Fellowship program. MAK also acknowledges the important collaborative contributions of theoretical groups involved in the projects in his laboratory in the USA, Brazil, Australia, and Europe.

DSS acknowledges the support of the US Department of Energy, Office of Science, Division of Chemical Sciences of the Office of Basic Energy Sciences under Contract DE-AC02-05CH11231, for the work performed at Lawrence Berkeley National Laboratory.

SD acknowledges the support from the FWF, Vienna, Austria (P30332 and I5390).

Authors contributions

All authors contributed equally.

References

1. C.C.J. Roothaan, Rev. Mod. Phys. **23**, 69 (1951) https://doi.org/10.1103/RevModPhys.23.69
2. T.N. Rescigno, I. B. H. Lengsfield , C.W. McCurdy, in *Modern Electronic Structure Theory: Part I*, ed. by D.R. Yarkony (World Scientific, Singapore, 1995), p. 501 https://doi.org/10.1142/9789812832108_0009
3. R.F. da Costa, M.T. do N. Varella, M.H.F. Bettega, M.A.P. Lima, Eur. Phys. J. D **69**, 159 (2015) https://doi.org/10.1140/epjd/e2015-60192-6
4. J. Tennyson, Phys. Rep. **491**, 29 (2010) https://doi.org/10.1016/j.physrep.2010.02.001
5. F.A. Gianturco, R.R. Lucchese, J. Phys. Chem. A **108**, 7056 (2004) https://doi.org/10.1021/jp049237y
6. M. Polášek, M. Juřek, M. Ingr, P. Čársky, J. Horáček, Phys. Rev. A **61**, 032701 (2000) https://doi.org/10.1103/PhysRevA.61.032701
7. F.A. Gianturco, R.R. Lucchese, N. Sanna, J. Chem. Phys. **102**, 5743 (1995) https://doi.org/10.1063/1.469305
8. P. Rawat, M.G.P. Homem, R.T. Sugohara, I.P. Sanches, I. Iga, G.L.C. de Souza, A.S. dos Santos, R.R. Lucchese, L.E. Machado, L.M. Brescansin, J. Phys. B: At. Mol. Opt. Phys. **43**, 225202 (2010) https://doi.org/10.1088/0953-4075/43/22/225202
9. F. Blanco, L. Ellis-Gibbings, G. García, Chem. Phys. Lett. **645**, 71 (2016) https://doi.org/10.1016/j.cplett.2015.11.056
10. B. Goswami, R. Naghma, B. Antony, Int. J. Mass Spectrom. **372**, 8 (2014) https://doi.org/10.1016/j.ijms.2014.08.018
11. T.-C. Jagau, K.B. Bravaya, A.I. Krylov, Ann. Rev. Phys. Chem. **68**, 525 (2017) https://doi.org/10.1146/annurev-physchem-052516-050622
12. K.D. Jordan, V.K. Voora, J. Simons, Theor. Chem. Acc. **133**, 1445 (2014) https://doi.org/10.1007/s00214-014-1445-1
13. I.I. Fabrikant, S. Eden, N.J. Mason, J. Fedor, in *Advances In Atomic, Molecular, and Optical Physics*, ed. by E. Arimondo, C.C. Lin, S.F. Yelin (Academic Press, 2017), p. 545 https://doi.org/10.1016/bs.aamop.2017.02.002
14. W. Domcke, Phys. Rep. **208**, 97 (1991) https://doi.org/10.1016/0370-1573(91)90125-6

15. A. Schramm, I.I. Fabrikant, J.M. Weber, E. Leber, M.W. Ruf, H. Hotop, J. Phys. B: At. Mol. Opt. Phys. **32**, 2153 (1999) https://doi.org/10.1088/0953-4075/32/9/307
16. M. Allan, M. Čížek, J. Horáček, W. Domcke, J. Phys. B: At. Mol. Opt. Phys. **33**, L209 (2000) https://doi.org/10.1088/0953-4075/33/6/103
17. M. Zawadzki, M. Čížek, K. Houfek, R. Čurík, M. Ferus, S. Civiš, J. Kočišek, J. Fedor, Phys. Rev. Lett. **121**, 143402 (2018) https://doi.org/10.1103/PhysRevLett.121.143402
18. G.A. Gallup, I.I. Fabrikant, Phys. Rev. A **83**, 012706 (2011) https://doi.org/10.1103/PhysRevA.83.012706
19. I.I. Fabrikant, Phys. Rev. A **43**, 3478 (1991) https://doi.org/10.1103/PhysRevA.43.3478
20. R.S. Wilde, G.A. Gallup, I.I. Fabrikant, J. Phys. B: At. Mol. Opt. Phys. **33**, 5479 (2000) https://doi.org/10.1088/0953-4075/33/24/302
21. W. Domcke, J. Phys. B: At. Mol. Opt. Phys. **14**, 4889 (1981) https://doi.org/10.1088/0022-3700/14/24/022
22. J. Horáček, M. Čížek, K. Houfek, P. Kolorenč, W. Domcke, Phys. Rev. A **70**, 052712 (2004) https://doi.org/10.1103/PhysRevA.70.052712
23. D.J. Haxton, Z. Zhang, H.-D. Meyer, T.N. Rescigno, C.W. McCurdy, Phys. Rev. A **69**, 062714 (2004) https://doi.org/10.1103/PhysRevA.69.062714
24. D.J. Haxton, C.W. McCurdy, T.N. Rescigno, Phys. Rev. A **73**, 062724 (2006) https://doi.org/10.1103/PhysRevA.73.062724
25. D.J. Haxton, C.W. McCurdy, T.N. Rescigno, Phys. Rev. A **75**, 012710 (2007); Erratum **76**, 049906 (2007) https://doi.org/10.1103/PhysRevA.75.012710
26. D.S. Slaughter, A. Belkacem, C.W. McCurdy, T.N. Rescigno, D.J. Haxton, J. Phys. B: At. Mol. Opt. Phys. **49**, 222001 (2016) https://doi.org/10.1088/0953-4075/49/22/222001
27. I.I. Fabrikant, J. Phys.: Conf. Ser. **204**, 012004 (2010) https://doi.org/10.1088/1742-6596/204/1/012004
28. M. Smyth, J. Kohanoff, I.I. Fabrikant, J. Chem. Phys. **140**, 184313 (2014) https://doi.org/10.1063/1.4874841
29. G.A. Worth, H.-D. Meyer, H. Köppel, L.S. Cederbaum, I. Burghardt, Int. Rev. Phys. Chem. **27**, 569 (2008) https://doi.org/10.1080/01442350802137656
30. S. Goursaud, M. Sizun, F. Fiquet-Fayard, J. Chem. Phys. **65**, 5453 (1976) https://doi.org/10.1063/1.433003
31. L. Lehr, W.H. Miller, Chem. Phys. Lett. **250**, 515 (1996) https://doi.org/10.1016/0009-2614(96)00037-1
32. L. Lehr, J. Manz, W.H. Miller, Chem. Phys. **214**, 301 (1997) https://doi.org/10.1016/S0301-0104(96)00311-4
33. C.W. McCurdy, J.L. Turner, J. Chem. Phys. **78**, 6773 (1983) https://doi.org/10.1063/1.444677
34. R. Crespo-Otero, M. Barbatti, Chem. Rev. **118**, 7026 (2018) https://doi.org/10.1021/acs.chemrev.7b00577
35. J.C. Tully, R.K. Preston, J. Chem. Phys. **55**, 562 (1971) https://doi.org/10.1063/1.1675788
36. J.C. Tully, J. Chem. Phys. **93**, 1061 (1990) https://doi.org/10.1063/1.459170
37. M. Ben-Nun, J. Quenneville, T.J. Martínez, J. Phys. Chem. A **104**, 5161 (2000) https://doi.org/10.1021/jp994174i

38. F. Kossoski, M.T. do N. Varella, M. Barbatti, J. Chem. Phys. **151**, 224104 (2019) https://doi.org/10.1063/1.5130547
39. F. Kossoski, M. Barbatti, Chem. Sci. **11**, 9827 (2020) https://doi.org/10.1039/D0SC04197A
40. L.M. Cornetta, T.J. Martinez, M.T. do N. Varella, Phys. Chem. Chem. Phys. **24**, 6845 (2022) https://doi.org/10.1039/D1CP05663H
41. M. Barbatti, WIREs Comput. Mol. Sci. **1**, 620 (2011) https://doi.org/10.1002/wcms.64
42. P.L. Gertitschke, W. Domcke, Phys. Rev. A **47**, 1031 (1993) https://doi.org/10.1103/PhysRevA.47.1031
43. R. Crespo-Otero, M. Barbatti, Theor. Chem. Acc. **131**, 1237 (2012) https://doi.org/10.1007/s00214-012-1237-4
44. D.M. Pearl, P.D. Burrow, J. Chem. Phys. **101**, 2940 (1994) https://doi.org/10.1063/1.467606
45. M. Barbatti, M. Ruckenbauer, F. Plasser, J. Pittner, G. Granucci, M. Persico, H. Lischka, WIREs Comput. Mol. Sci. **4**, 26 (2014) https://doi.org/10.1002/wcms.1158
46. J.K. Olthoff, J.A. Tossell, J.H. Moore, J. Chem. Phys. **83**, 5627 (1985) https://doi.org/10.1063/1.449687
47. E.J. Heller, J. Chem. Phys. **75**, 2923 (1981) https://doi.org/10.1063/1.442382
48. F. Kossoski, M.T. do N. Varella, Phys. Chem. Chem. Phys. **17**, 17271 (2015) https://doi.org/10.1039/C5CP01475A
49. H. Abdoul-Carime, M.A. Huels, F. Brüning, E. Illenberger, L. Sanche, J. Chem. Phys. **113**, 2517 (2000) https://doi.org/10.1063/1.1306654
50. M. Zawadzki, R. Wright, G. Dolmat, M.F. Martin, L. Hargreaves, D.V. Fursa, M.C. Zammit, L.H. Scarlett, J.K. Tapley, J.S. Savage, I. Bray, M.A. Khakoo, Phys. Rev. A **97**, 050702 (2018) https://doi.org/10.1103/physreva.97.050702
51. M. Zawadzki, R. Wright, G. Dolmat, M.F. Martin, B. Diaz, L. Hargreaves, D. Coleman, D.V. Fursa, M.C. Zammit, L.H. Scarlett, J.K. Tapley, J.S. Savage, I. Bray, M.A. Khakoo, Phys. Rev. A **98**, 062704 (2018) https://doi.org/10.1103/physreva.98.062704
52. J. Muse, H. Silva, M.C.A. Lopes, M.A. Khakoo, J. Phys. B: At. Mol. Opt. Phys. **41**, 095203 (2008) https://doi.org/10.1088/0953-4075/41/9/095203
53. L.R. Hargreaves, S. Bhari, B. Adjari, X. Liu, R. Laher, M. Zammit, J.S. Savage, D.V. Fursa, I. Bray, M.A. Khakoo, J. Phys. B: At. Mol. Opt. Phys. **50**, 225203 (2017) https://doi.org/10.1088/1361-6455/aa9048
54. M.A. Khakoo, C.E. Beckmann, S. Trajmar, G. Csanak, J. Phys. B: At. Mol. Opt. Phys. **27**, 3159 (1994) https://doi.org/10.1088/0953-4075/27/14/045
55. M.A. Khakoo, K. Keane, C. Campbell, N. Guzman, K. Hazlett, J. Phys. B: At. Mol. Opt. Phys. **40**, 3601 (2007) https://doi.org/10.1088/0953-4075/40/18/003
56. M. Zawadzki, M.A. Khakoo, L. Voorneman, L. Ratkovich, Z. Măsín, K. Houfek, A. Dora, R. Laher, J. Tennyson, J. Phys. B: At. Mol. Opt. Phys. **53**, 165201 (2020) https://doi.org/10.1088/1361-6455/ab95ef
57. J. Zobel, U. Mayer, K. Jung, H. Ehrhardt, J. Phys. B: At. Mol. Opt. Phys. **29**, 813 (1996) https://doi.org/10.1088/0953-4075/29/4/021
58. P.W. Zetner, I. Kanik, S. Trajmar, J. Phys. B: At. Mol. Opt. Phys. **31**, 2395 (1998) https://doi.org/10.1088/0953-4075/31/10/025
59. A.G. Middleton, M.J. Brunger, P.J.O. Teubner, J. Phys. B: At. Mol. Opt. Phys. **26**, 1743 (1993) https://doi.org/10.1088/0953-4075/26/11/009

60. Z. Mašín, J. Benda, J.D. Gorfinkiel, A.G. Harvey, J. Tennyson, Comput. Phys. Commun. **249**, 107092 (2020) https://doi.org/10.1016/j.cpc.2019.107092
61. Q. Sun, C. Winstead, V. Mckoy, Phys. Rev. A **46**, 6987 (1992) https://doi.org/10.1103/physreva.46.6987
62. M. Zawadzki, M.A. Khakoo, A. Sakaamini, L. Voorneman, L. Ratkovich, Z. Măsín, A. Dora, R. Laher, J. Tennyson, J. Phys. B: At. Mol. Opt. Phys. **55**, 025201 (2022) https://doi.org/10.1088/1361-6455/ac37f3
63. A. Sakaamini, J.-B. Faure, M.A. Khakoo, O.I. Zatsarinny, K. Bartschat, Atoms **9**, 61 (2021) https://doi.org/10.3390/atoms9030061
64. X. Guo, D.F. Mathews, G. Mikaelian, M.A. Khakoo, A. Crowe, I. Kanik, S. Trajmar, V. Zeman, K. Bartschat, C.J. Fontes, J. Phys. B: At. Mol. Opt. Phys. **33**, 1895 (2000) https://doi.org/10.1088/0953-4075/33/10/306
65. L.R. Hargreaves, C. Campbell, M.A. Khakoo, O. Zatsarinny, K. Bartschat, Phys. Rev. A **85**, 050701 (2012) https://doi.org/10.1103/physreva.85.050701
66. A. Sakaamini, J.B. Faure, M.A. Khakoo, O. Zatsarinny, K. Bartschat, Phys. Rev. A **104**, 062805 (2021) https://doi.org/10.1103/PhysRevA.104.062805
67. B.A. Hlousek, M.F. Martin, M.A. Khakoo, M. Zawadzki, G.M. Moreira, L.S. Maioli, M.H.F. Bettega, L.E. Machado, V.A.S. da Mata, A.J. da Silva, I. Iga, M.T. Lee, M.G.P. Homem, Phys. Rev. A **100**, 052709 (2019) https://doi.org/10.1103/PhysRevA.100.052709
68. B.A. Hlousek, M.F. Martin, M. Zawadzki, M.A. Khakoo, L.E. Machado, R.R. Lucchese, V.A.S. Da Mata, I. Iga, M.-T. Lee, M.G.P. Homem, J. Phys. B: At. Mol. Opt. Phys. **52**, 025204 (2019) https://doi.org/10.1088/1361-6455/aaf2f4
69. J.N.H. Brunt, G.C. King, F.H. Read, J. Phys. B: Atom. Mol. Phys. **10**, 433 (1977) https://doi.org/10.1088/0022-3700/10/3/012
70. S.G. Lias, in *NIST Chemistry WebBook, NIST Standard Reference Database Number 69*, ed. by P.J. Linstrom, W.G. Mallard (National Institute of Standards and Technology, Gaithersburg MD), p. 20899 https://webbook.nist.gov/cgi/cbook.cgi?ID=C67663&Mask=20#Ion-Energetics
71. A. Sakaamini, S.M. Khakoo, L. Hargreaves, M.A. Khakoo, D.F. Pastega, M.H.F. Bettega, Phys. Rev. A **95**, 022702 (2017) https://doi.org/10.1103/physreva.95.022702
72. J.L. Wiza, Nucl. Instrum. Methods **162**, 587 (1979) https://doi.org/10.1016/0029-554X(79)90734-1
73. O. Jagutzki, V. Mergel, K. Ullmann-Pfleger, L. Spielberger, U. Meyer, R. Dörner, H.W. Schmidt-Boecking, in Proc. SPIE 3438, Imaging Spectrometry IV, ed. by M.R. Descour, S.S. Shen (San Diego, CA, USA, 1998), p. 322 https://doi.org/10.1117/12.328113
74. G.J. Schulz, Rev. Mod. Phys. **45**, 423 (1973) https://doi.org/10.1103/RevModPhys.45.423
75. G.H. Dunn, L. Kieffer, Phys. Rev. **132**, 2109 (1963) https://doi.org/10.1103/PhysRev.132.2109
76. R. Van Brunt, L. Kieffer, Phys. Rev. A **2**, 1899 (1970) https://doi.org/10.1103/PhysRevA.2.1899
77. M.J. Brunger, S.J. Buckman, Phys. Rep. **357**, 215 (2002) https://doi.org/10.1016/S0370-1573(01)00032-1
78. T. Oster, A. Kühn, E. Illenberger, Int. J. Mass Spectrom. Ion Phys. **89**, 1 (1989) https://doi.org/10.1016/0168-1176(89)85031-1

79. H. Hotop, M.-W. Ruf, M. Allan, I.I. Fabrikant, in *Advances In Atomic, Molecular, and Optical Physics*, ed. by B. Bederson, H. Walther (Academic Press, 2003), p. 85 https://doi.org/10.1016/S1049-250X(03)80004-6
80. K. Jung, E. Schubert, D. Paul, H. Ehrhardt, J. Phys. B: Atom. Mol. Phys. **8**, 1330 (1975) https://doi.org/10.1088/0022-3700/8/8/024
81. D. Milne-Brownlie, M. Foster, J. Gao, B. Lohmann, D. Madison, Phys. Rev. Lett. **96**, 233201 (2006) https://doi.org/10.1103/PhysRevLett.96.233201
82. M.J. Hussey, A.J. Murray, . Phys. B: At. Mol. Opt. Phys. **35**, 3399 (2002) https://doi.org/10.1088/0953-4075/35/16/303
83. A. Lahmam-Bennani, A. Naja, E.S. Casagrande, N. Okumus, C. Dal Cappello, I. Charpentier, S. Houamer, J. Phys. B: At. Mol. Opt. Phys. **42**, 165201 (2009) https://doi.org/10.1088/0953-4075/42/16/165201
84. M. Takahashi, N. Watanabe, Y. Khajuria, Y. Udagawa, J. Eland, Phys. Rev. Lett. **94**, 213202 (2005) https://doi.org/10.1103/PhysRevLett.94.213202
85. J. Ullrich, R. Moshammer, A. Dorn, R. Dörner, L.P.H. Schmidt, H. Schmidt-Böcking, Rep. Prog. Phys. **66**, 1463 (2003) https://doi.org/10.1088/0034-4885/66/9/203
86. E. Krishnakumar, V.S. Prabhudesai, in *Quantum Collisions and Confinement of Atomic and Molecular Species, and Photons*, ed. by P. Deshmukh, et al. (Springer, Singapore, 2019), p. 20
87. D.W. Chandler, P.L. Houston, J. Chem. Phys. **87**, 1445 (1987) https://doi.org/10.1063/1.453276
88. A.J. Heck, D.W. Chandler, Annu. Rev. Phys. Chem. **46**, 335 (1995) https://doi.org/10.1146/annurev.pc.46.100195.002003
89. P.L. Houston, J. Phys. Chem. **100**, 12757 (1996) https://doi.org/10.1021/jp960131f
90. D.W. Chandler, P.L. Houston, D.H. Parker, J. Chem. Phys. **147**, 013601 (2017) https://doi.org/10.1063/1.4983623
91. R.F. Delmdahl, B.L. Bakker, D.H. Parker, J. Chem. Phys. **113**, 7728 (2000) https://doi.org/10.1063/1.1321771
92. A.T. Eppink, D.H. Parker, Rev. Sci. Instrum. **68**, 3477 (1997) https://doi.org/10.1063/1.1148310
93. H.B. Michaelson, J. Appl. Phys. **48**, 4729 (1977) https://doi.org/10.1063/1.323539
94. D. Nandi, V.S. Prabhudesai, E. Krishnakumar, A. Chatterjee, Rev. Sci. Instrum. **76**, 053107 (2005) https://doi.org/10.1063/1.1899404
95. B. Wu, L. Xia, H.-K. Li, X.-J. Zeng, S. Xi Tian, Rev. Sci. Instrum. **83**, 013108 (2012) https://doi.org/10.1063/1.3678328
96. H. Adaniya, D. Slaughter, T. Osipov, T. Weber, A. Belkacem, Rev. Sci. Instrum. **83**, 023106 (2012) https://doi.org/10.1063/1.3685244
97. A. Moradmand, J. Williams, A. Landers, M. Fogle, Rev. Sci. Instrum. **84**, 033104 (2013) https://doi.org/10.1063/1.4794093
98. T. Rescigno, C. Trevisan, A. Orel, D. Slaughter, H. Adaniya, A. Belkacem, M. Weyland, A. Dorn, C. McCurdy, Phys. Rev. A **93**, 052704 (2016) https://doi.org/10.1103/PhysRevA.93.052704
99. E. Wang, X. Shan, L. Chen, T. Pfeifer, X. Chen, X. Ren, A. Dorn, J. Phys. Chem. A **124**, 2785 (2020) https://doi.org/10.1021/acs.jpca.0c02074

100. X. Ren, E. Wang, A.D. Skitnevskaya, A.B. Trofimov, K. Gokhberg, A. Dorn, Nat. Phys. **14**, 1062 (2018) https://doi.org/10.1038/s41567-018-0214-9
101. G. Panelli, A. Moradmand, B. Griffin, K. Swanson, T. Weber, T.N. Rescigno, C.W. McCurdy, D.S. Slaughter, J.B. Williams, Phys. Rev. Res. **3**, 013082 (2021) https://doi.org/10.1103/PhysRevResearch.3.013082
102. T. Hamann, A. Edtbauer, F.F. Da Silva, S. Denifl, P. Scheier, P. Swiderek, Phys. Chem. Chem. Phys. **13**, 12305 (2011) https://doi.org/10.1039/C1CP20833K
103. A. Moradmand, D. Slaughter, D. Haxton, T. Rescigno, C. McCurdy, T. Weber, S. Matsika, A. Landers, A. Belkacem, M. Fogle, Phys. Rev. A **88**, 032703 (2013) https://doi.org/10.1103/PhysRevA.88.032703
104. P. Nag, M. Polášek, J. Fedor, Phys. Rev. A **99**, 052705 (2019) https://doi.org/10.1103/PhysRevA.99.052705
105. P. Nag, M. Tarana, J. Fedor, Phys. Rev. A **103**, 032830 (2021) https://doi.org/10.1103/PhysRevA.103.032830
106. X. Ren, E. Jabbour Al Maalouf, A. Dorn, S. Denifl, Nat. Commun. **7**, 11093 (2016) https://doi.org/10.1038/ncomms11093
107. H.J. Svec, Int. J. Mass Spectrom. Ion Process. **66**, 3 (1985) https://doi.org/10.1016/0168-1176(85)83017-2
108. F.W. McLafferty, J. Pinzelik, Anal. Chem. **38**, 350 (1966) https://doi.org/10.1021/ac60237a024
109. Z. Li, A.R. Milosavljević, I. Carmichael, S. Ptasinska, Phys. Rev. Lett. **119**, 053402 (2017) https://doi.org/10.1103/PhysRevLett.119.053402
110. F.P. Lossing, Ann. N. Y. Acad. Sci. **67**, 499 (1957) https://doi.org/10.1111/j.1749-6632.1957.tb46074.x
111. D. Beck, O. Osberghaus, Z. Physik **160**, 406 (1960) https://doi.org/10.1007/BF01322104
112. D. Beck, Discuss. Faraday Soc. **36**, 56 (1963) https://doi.org/10.1039/DF9633600056
113. G.D. Flesch, H.J. Svec, Int. J. Mass Spectrom. Ion Process. **56**, 93 (1984) https://doi.org/10.1016/0168-1176(84)85035-1
114. C.E. Melton, J. Chem. Phys. **45**, 4414 (1966) https://doi.org/10.1063/1.1727520
115. C.E. Melton, J. Phys. Chem. **74**, 582 (1970) https://doi.org/10.1021/j100698a017
116. C.E. Melton, J. Sci. Instrum. **43**, 927 (1966) https://doi.org/10.1088/0950-7671/43/12/312
117. J.R. Reeher, G.D. Flesch, H.J. Svec, Org. Mass Spectrom. **11**, 154 (1976) https://doi.org/10.1002/oms.1210110210
118. G.D. Flesch, H.J. Svec, Int. J. Mass Spectrom. Ion Process. **59**, 295 (1984) https://doi.org/10.1016/0168-1176(84)85103-4
119. G.D. Flesch, R.E. Utecht, H.J. Svec, Int. J. Mass Spectrom. Ion Process. **58**, 151 (1984) https://doi.org/10.1016/0168-1176(84)80025-7
120. J.R. Reeher, G.D. Flesch, H.J. Svec, Int. J. Mass Spectrom. Ion Phys. **19**, 351 (1976) https://doi.org/10.1016/0020-7381(76)80019-8
121. G.D. Flesch, H.J. Svec, Int. J. Mass Spectrom. Ion Phys. **38**, 361 (1981) https://doi.org/10.1016/0020-7381(81)80081-2
122. T. Nakano, H.T.H. Toyoda, H.S.H. Sugai, Jpn. J. Appl. Phys. **30**, 2908 (1991) https://doi.org/10.1143/JJAP.30.2908

123. T. Nakano, H.T.H. Toyoda, H.S.H. Sugai, Jpn. J. Appl. Phys. **30**, 2912 (1991) https://doi.org/10.1143/JJAP.30.2912
124. T. Nakano, H. Sugai, Jpn. J. Appl. Phys. **31**, 2919 (1992) https://doi.org/10.1143/JJAP.31.2919
125. T. Nakano, H. Sugai, J.Phys. D: Appl. Phys. **26**, 1909 (1993) https://doi.org/10.1088/0022-3727/26/11/011
126. E.R. Fisher, B.L. Kickel, P.B. Armentrout, J. Chem. Phys. **97**, 4859 (1992) https://doi.org/10.1063/1.463840
127. M. Iio, M. Goto, H. Toyoda, H. Sugai, Contrib. Plasma Phys. **35**, 405 (1995) https://doi.org/10.1002/ctpp.2150350408
128. L.G. Christophorou, J.K. Olthoff, J. Phys. Chem. Ref. Data **29**, 267 (2000) https://doi.org/10.1063/1.1288407
129. H. Sugai, H. Toyoda, J. Vac. Sci. Technol. A **10**, 1193 (1992) https://doi.org/10.1116/1.578226
130. J. Benedikt, H. Kersten, A. Piel, Plasma Sources Sci. Technol. **30**, 033001 (2021) https://doi.org/10.1088/1361-6595/abe4bf
131. R.N. Compton, J.N. Bardsley, in *Electron-Molecule Collisions*, ed. by I. Shimamura, K. Takayanagi (Springer US, Boston, MA, 1984), p. 275 https://doi.org/10.1007/978-1-4613-2357-0_4
132. M. Bazin, S. Ptasinska, A.D. Bass, L. Sanche, E. Burean, P. Swiderek, J. Phys.: Condens. Matter **22**, 084003 (2010) https://doi.org/10.1088/0953-8984/22/8/084003
133. Y. Chen, A. Aleksandrov, T.M. Orlando, Int. J. Mass Spectrom. **277**, 314 (2008) https://doi.org/10.1016/j.ijms.2008.07.003
134. J.W. McConkey, W. Kedzierski, in *Adv. Atom. Mol. Opt. Phys.*, ed. by E. Arimondo, P.R. Berman, C.C. Lin (Academic Press, 2014), p. 1 https://doi.org/10.1016/B978-0-12-800129-5.00001-8
135. J.M. Dech, W. Kedzierski, J.W. McConkey, J. Phys. B: At. Mol. Opt. Phys. **53**, 155204 (2020) https://doi.org/10.1088/1361-6455/ab94c7
136. C.J. Tiessen, J.A. Trocchi, J.D. Hein, J. Dech, W. Kedzierski, J.W. McConkey, J. Phys. B: At. Mol. Opt. Phys. **49**, 125204 (2016) https://doi.org/10.1088/0953-4075/49/12/125204
137. J.A. Trocchi, J. Dech, W. Kedzierski, J.W. McConkey, J. Phys. B: At. Mol. Opt. Phys. **52**, 055204 (2019) https://doi.org/10.1088/1361-6455/ab0222
138. S. Ptasińska, S. Denifl, B. Mróz, M. Probst, V. Grill, E. Illenberger, P. Scheier, T.D. Märk, J. Chem. Phys. **123**, 124302 (2005) https://doi.org/10.1063/1.2035592
139. S. Denifl, P. Sulzer, D. Huber, F. Zappa, M. Probst, T.D. Märk, P. Scheier, N. Injan, J. Limtrakul, R. Abouaf, H. Dunet, Angew. Chem. Int. Ed. **46**, 5238 (2007) https://doi.org/10.1002/anie.200700032
140. T. Harb, W. Kedzierski, J.W. McConkey, J. Chem. Phys. **115**, 5507 (2001) https://doi.org/10.1063/1.1397327
141. R.S. Berry, H. Haberland, in *Clusters of Atoms and Molecules* (Springer, Berlin, Heidelberg, 1994) https://doi.org/10.1007/978-3-642-84329-7_1
142. R.L. Johnston, *Atomic and Molecular Clusters*. (CRC Press London, UK, 2002) https://doi.org/10.1201/9781482289305

143. J. Jortner, Ber. Bunsenges. Phys. Chem. **88**, 188 (1984) https://doi.org/10.1002/bbpc.19840880303
144. J.P. Toennies, A.F. Vilesov, Angew. Chem. Int. Ed. **43**, 2622 (2004) https://doi.org/10.1002/anie.200300611
145. J.D. Gorfinkiel, S. Ptasinska, J. Phys. B: At. Mol. Opt. Phys. **50**, 182001 (2017) https://doi.org/10.1088/1361-6455/aa8572
146. I. Bald, J. Langer, P. Tegeder, O. Ingólfsson, Int. J. Mass Spectrom. **277**, 4 (2008) https://doi.org/10.1016/j.ijms.2008.06.013
147. H. Haberland, U. Buck, G. Scoles, in *Clusters of Atoms and Molecules*, ed. by H. Haberland (Springer, Berlin, Heidelberg, 1994), p. 207 https://doi.org/10.1007/978-3-642-84329-7_3
148. M.D. Morse, in *Atomic, Molecular, and Optical Physics: Atoms and Molecules*, ed. by F.B. Dunning, R.G. Hulet (Academic Press, San Diego, CA, 1996), p. 21 https://doi.org/10.1016/S0076-695X(08)60784-X
149. O.F. Hagena, Rev. Sci. Instrum. **63**, 2374 (1992) https://doi.org/10.1063/1.1142933
150. M. Neustetter, J. Aysina, F.F. da Silva, S. Denifl, Angew. Chem. Int. Ed. **54**, 9124 (2015) https://doi.org/10.1002/anie.201503733
151. M. Neustetter, M. Mahmoodi-Darian, S. Denifl, J. Am. Soc. Mass Spectrom. **28**, 866 (2017) https://doi.org/10.1007/s13361-017-1634-y
152. E. Illenberger, Chem. Rev. **92**, 1589 (1992) https://doi.org/10.1021/cr00015a006
153. E. Leber, S. Barsotti, I.I. Fabrikant, J.M. Weber, M.-W. Ruf, H. Hotop, Eur. Phys. J. D **12**, 125 (2000) https://doi.org/10.1007/s100530070049
154. M. Braun, I.I. Fabrikant, M.-W. Ruf, H. Hotop, J. Phys. B: At. Mol. Opt. Phys. **46**, 195202 (2013) https://doi.org/10.1088/0953-4075/46/19/195202
155. S. Denifl, F. Zappa, A. Mauracher, F. Ferreira da Silva, A. Bacher, O. Echt, T.D. Märk, D.K. Bohme, P. Scheier, ChemPhysChem **9**, 1387 (2008) https://doi.org/10.1002/cphc.200800245
156. S. Denifl, F. Zappa, I. Mähr, A. Mauracher, M. Probst, T.D. Märk, P. Scheier, J. Am. Chem. Soc. **130**, 5065 (2008) https://doi.org/10.1021/ja075972m
157. V. Periquet, A. Moreau, S. Carles, J.P. Schermann, C. Desfrancois, J. El. Spect. Rel. Phen. **106**, 141 (2000) https://doi.org/10.1016/S0368-2048(99)00072-9
158. M. Seydou, A. Modelli, B. Lucas, K. Konate, C. Desfrançois, J.P. Schermann, Eur. Phys. J. D **35**, 199 (2005) https://doi.org/10.1140/epjd/e2005-00089-5
159. R. Meißner, J. Kočišek, L. Feketeová, J. Fedor, M. Fárník, P. Limão-Vieira, E. Illenberger, S. Denifl, Nat. Commun. **10**, 2388 (2019) https://doi.org/10.1038/s41467-019-10340-8
160. M. Ončák, R. Meißner, E. Arthur-Baidoo, S. Denifl, T.F.M. Luxford, A. Pysanenko, M. Fárník, J. Pinkas, J. Kočišek, Int. J. Mol. Sci. **20**, 4383 (2019) https://doi.org/10.3390/ijms20184383
161. J. Kocisek, A. Pysanenko, M. Fárník, J. Fedor, J. Phys. Chem. Lett. **7**, 3401 (2016) https://doi.org/10.1021/acs.jpclett.6b01601
162. X. Ren, E. Jabbour Al Maalouf, A. Dorn, S. Denifl, Nat. Commun. **7**, 11093 (2016) https://doi.org/10.1038/ncomms11093
163. D.I. Edwards, J. Antimicrob. Chemother. **31**, 9 (1993) https://doi.org/10.1093/jac/31.1.9
164. R. Meißner, L. Feketeová, A. Bayer, P. Limão-Vieira, S. Denifl, J. Chem. Phys. **154**, 074306 (2021) https://doi.org/10.1063/5.0040045

165. R. Meißner, L. Feketeová, E. Illenberger, S. Denifl, Int. J. Mol. Sci. **20**, 3496 (2019) https://doi.org/10.3390/ijms20143496
166. K. Tanzer, L. Feketeová, B. Puschnigg, P. Scheier, E. Illenberger, S. Denifl, Angew. Chem. Int. Ed. **53**, 12240 (2014) https://doi.org/10.1002/anie.201407452
167. A. Ribar, K. Fink, M. Probst, S.E. Huber, L. Feketeová, S. Denifl, Chem. Eur. J. **23**, 12892 (2017) https://doi.org/10.1002/chem.201702644
168. F. Kossoski, M.T. do N Varella, J. Chem. Phys. **147**, 164310 (2017) https://doi.org/10.1063/1.5005604
169. D. Almeida, D. Kinzel, F.F. da Silva, B. Puschnigg, D. Gschliesser, P. Scheier, S. Denifl, G. García, L. González, P. Limão-Vieira, Phys. Chem. Chem. Phys. **15**, 11431 (2013) https://doi.org/10.1039/C3CP50548K
170. L. Feketeová, A.L. Albright, B.S. Sørensen, M.R. Horsman, J. White, R.A.J. O'Hair, N. Bassler, Int. J. Mass Spectrom. **365**, 56 (2014) https://doi.org/10.1016/j.ijms.2013.12.014
171. J.V. Coe, S.T. Arnold, J.G. Eaton, G.H. Lee, K.H. Bowen, J. Chem. Phys. **125**, 014315 (2006) https://doi.org/10.1063/1.2212415
172. M.-Y. Song, H. Cho, G.P. Karwasz, V. Kokoouline, Y. Nakamura, J. Tennyson, A. Faure, N.J. Mason, Y. Itikawa, J. Phys. Chem. Ref. Data **50**, 023103 (2021) https://doi.org/10.1063/5.0035315
173. B. Boudaïffa, P. Cloutier, D. Hunting, M.A. Huels, L. Sanche, Science **287**, 1658 (2000) https://doi.org/10.1126/science.287.5458.1658
174. X. Guo, D.F. Mathews, G. Mikaelian, M.A. Khakoo, A. Crowe, I. Kanik, S. Trajmar, V. Zeman, K. Bartschat, C.J. Fontes, J. Phys. B: At. Mol. Opt. Phys. **33**, 1921 (2000) https://doi.org/10.1088/0953-4075/33/10/307
175. E. Schow, K. Hazlett, J.G. Childers, C. Medina, G. Vitug, I. Bray, D.V. Fursa, M.A. Khakoo, Phys. Rev. A **72**, 062717 (2005) https://doi.org/10.1103/physreva.72.062717
176. H. Cho, R.J. Gulley, K. Sunohara, M. Kitajima, L.J. Uhlmann, H. Tanaka, S.J. Buckman, J. Phys. B: At. Mol. Opt. Phys. **34**, 1019 (2001) https://doi.org/10.1088/0953-4075/34/6/304
177. H. Kato, M. Hoshino, H. Tanaka, P. Limão-Vieira, O. Ingólfsson, L. Campbell, M.J. Brunger, J. Chem. Phys. **134**, 134308 (2011) https://doi.org/10.1063/1.3575497
178. T.P.T. Do, K.L. Nixon, M. Fuss, G. García, F. Blanco, M.J. Brunger, J. Chem. Phys. **136**, 184313 (2012) https://doi.org/10.1063/1.4716184
179. K. Ralphs, G. Serna, L.R. Hargreaves, M.A. Khakoo, C. Winstead, V. McKoy, J. Phys. B: At. Mol. Opt. Phys. **46**, 125201 (2013) https://doi.org/10.1088/0953-4075/46/12/125201
180. A. Zhao, M. van Beuzekom, B. Bouwens, D. Byelov, I. Chakaberia, C. Cheng, E. Maddox, A. Nomerotski, P. Svihra, J. Visser, Rev. Sci. Instrum. **88**, 113104 (2017) https://doi.org/10.1063/1.4996888
181. J. Postulka, P. Slavicek, J. Fedor, M. Fárník, J. Kocisek, J. Phys. Chem. B **121**, 8965 (2017) https://doi.org/10.1021/acs.jpcb.7b07390
182. E. Arthur-Baidoo, K. Falkiewicz, L. Chomicz-Mańka, A. Czaja, S. Demkowicz, K. Biernacki, W. Kozak, J. Rak, S. Denifl, Int. J. Mol. Sci. **22**, 2344 (2021) https://doi.org/10.3390/ijms22052344
183. P. Spisz, M. Zdrowowicz, W. Kozak, L. Chomicz-Mańka, K. Falkiewicz, S. Makurat, A. Sikorski, D. Wyrzykowski, J. Rak, E. Arthur-Baidoo, P. Ziegler, M.S.R. Costa, S. Denifl, J. Phys. Chem. B **124**, 5600 (2020) https://doi.org/10.1021/acs.jpcb.0c03844

184. R. Meißner, S. Makurat, W. Kozak, P. Limão-Vieira, J. Rak, S. Denifl, J. Phys. Chem. B **123**, 1274 (2019) https://doi.org/10.1021/acs.jpcb.8b11523
185. J. Ameixa, E. Arthur-Baidoo, R. Meißner, S. Makurat, W. Kozak, K. Butowska, F. Ferreira da Silva, J. Rak, S. Denifl, J. Chem. Phys. **149**, 164307 (2018) https://doi.org/10.1063/1.5050594
186. M. Johny, J. Onvlee, T. Kierspel, H. Bieker, S. Trippel, J. Küpper, Chem. Phys. Lett. **721**, 149 (2019) https://doi.org/10.1016/j.cplett.2019.01.052
187. J.V. Barnes, M. Beck, S. Hartweg, A. Luski, B.L. Yoder, J. Narevicius, E. Narevicius, R. Signorell, Phys. Chem. Chem. Phys. **23**, 846 (2021) https://doi.org/10.1039/D0CP04647G
188. J.B. Fenn, M. Mann, C.K. Meng, S.F. Wong, C.M. Whitehouse, Mass Spectrom. Rev. **9**, 37 (1990) https://doi.org/10.1002/mas.1280090103
189. B. Liu, N. Haag, H. Johansson, H.T. Schmidt, H. Cederquist, S. Brøndsted Nielsen, H. Zettergren, P. Hvelplund, B. Manil, B.A. Huber, J. Chem. Phys. **128**, 075102 (2008) https://doi.org/10.1063/1.2839597
190. H. Zettergren, L. Adoui, V. Bernigaud, H. Cederquist, N. Haag, A.I.S. Holm, B.A. Huber, P. Hvelplund, H. Johansson, U. Kadhane, M. Koefoed Larsen, B. Liu, B. Manil, S. Brøndsted Nielsen, S. Panja, J. Rangama, P. Reinhed, H.T. Schmidt, K. Støchkel, ChemPhysChem **10**, 1619 (2009) https://doi.org/10.1002/cphc.200800782
191. B. Liu, S. Brøndsted Nielsen, P. Hvelplund, H. Zettergren, H. Cederquist, B. Manil, B.A. Huber, Phys. Rev. Lett. **97**, 133401 (2006) https://doi.org/10.1103/PhysRevLett.97.133401
192. R.A. Zubarev, Curr. Opin. Biotechnol. **15**, 12 (2004) https://doi.org/10.1016/j.copbio.2003.12.002
193. K. Gokhberg, L.S. Cederbaum, Phys. Rev. A **82**, 052707 (2010) https://doi.org/10.1103/PhysRevA.82.052707
194. K. Gokhberg, L.S. Cederbaum, J. Phys. B: At. Mol. Opt. Phys. **42**, 231001 (2009) https://doi.org/10.1088/0953-4075/42/23/231001
195. A. Molle, A. Dubois, J.D. Gorfinkiel, L.S. Cederbaum, N. Sisourat, Phys. Rev. A **103**, 012808 (2021) https://doi.org/10.1103/PhysRevA.103.012808
196. A. Molle, A. Dubois, J.D. Gorfinkiel, L.S. Cederbaum, N. Sisourat, Phys. Rev. A **104**, 022818 (2021) https://doi.org/10.1103/PhysRevA.104.022818
197. N. Sisourat, T. Miteva, J.D. Gorfinkiel, K. Gokhberg, L.S. Cederbaum, Phys. Rev. A **98**, 020701(R) (2018) https://doi.org/10.1103/PhysRevA.98.020701

Fig. 1 DEA cross-sections for chloroethane. (a) cross-sections computed with 1400 (solid curve) and 100 (dashed curve) trajectories with the linewidth of 0.1 eV. (b) same as in (a), although with the linewidth of 0.5 eV. (c) cross-sections computed with different vertical resonance positions, i.e., 2.23, 2.33, and 2.43 eV (from the highest to the lowest peak). (d): same as in (c), although varying the vertical resonance width, i.e., 1.25, 1.35, and 1.45 eV (from the highest to the lowest peak). In all panels, the purple curves indicate the theoretical results, while the red curves are the experimental data (For details, see [38]). Reprinted from [38], with the permission of AIP Publishing

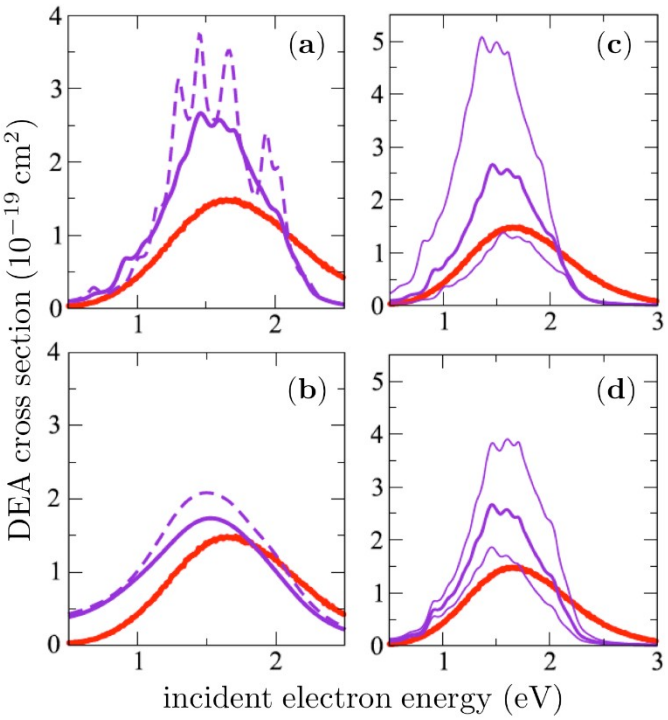
(a)
(b)
(c)
(d)
DEA cross section (10^{-19} cm^2)
incident electron energy (eV)

Fig. 2 Calculated (purple curve) and experimental (open circle) DEA cross-sections for iodoethene. The calculations employed 1600 trajectories and a phenomenological linewidth of 0.05 eV (left panel). Contributions from the adiabatic (blue curve) and non-adiabatic (red curve) DEA mechanisms (right panel). Reproduced from Ref. [39] with permission from the Royal Society of Chemistry

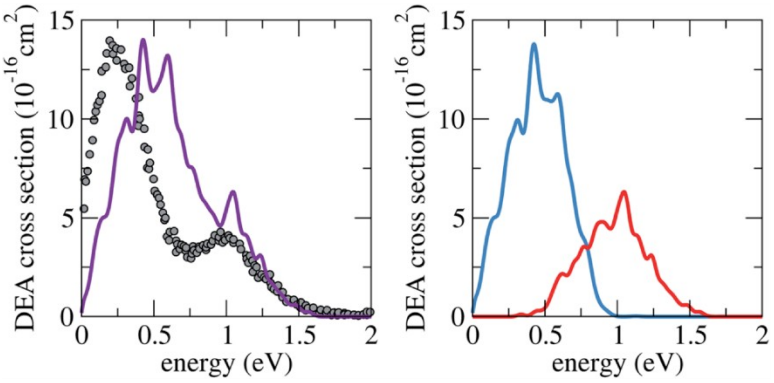

Fig. 3 Representative geometries of the $5BrU^-$ anion. The dynamics starts at the D_2 anionic state, having π_2^* character in most of the initial conditions (top left configuration). The system then undergoes D_2/D_1 and D_1/D_0 transitions (right configurations). The dynamics in the anionic ground state (D_0) was propagated up to 380 fs, and the final geometries are shown in the bottom left panel. The geometries were obtained from simulations on the real-valued potentials, not accounting for the survival probabilities. Reproduced from Ref. [40] with permission from the Royal Society of Chemistry

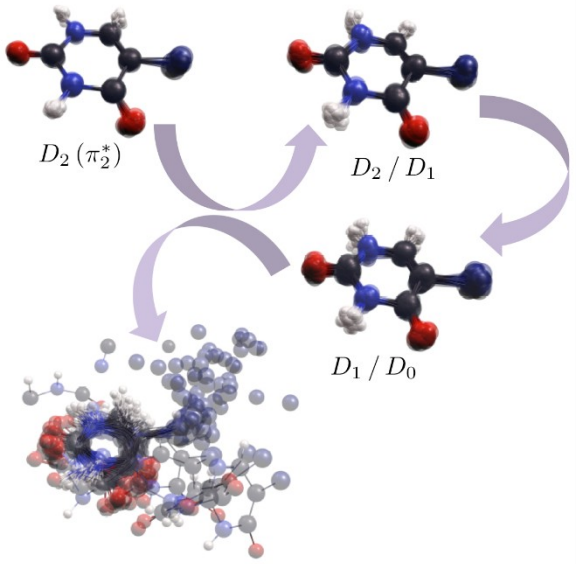

Fig. 4 (a) TOF background-subtracted electron scattering spectrum for H_2 (green circle) The curves are obtained by computer fitting of the whole spectrum (blue curve) decomposed into the $X^1\Sigma^+_g \rightarrow b^3\Sigma^+_u$ transition (red curve) and the higher-lying H_2 states (green curve). (b) Electron-impact excitation scattering DCS values (in atomic units) for exciting the $X^1\Sigma_g^+ \rightarrow b^3\Sigma_u^+$ transition at electron impact energy (E_0) of 20 eV obtained from the several experiments (red circle, green triangle, brown diamond, blue square), and computed using CCC (black curve) and SMC (green curve) methods (For details, see [51]. Both panels reprinted with permission from Ref. [51]. Copyright (2018) by the American Physical Society.

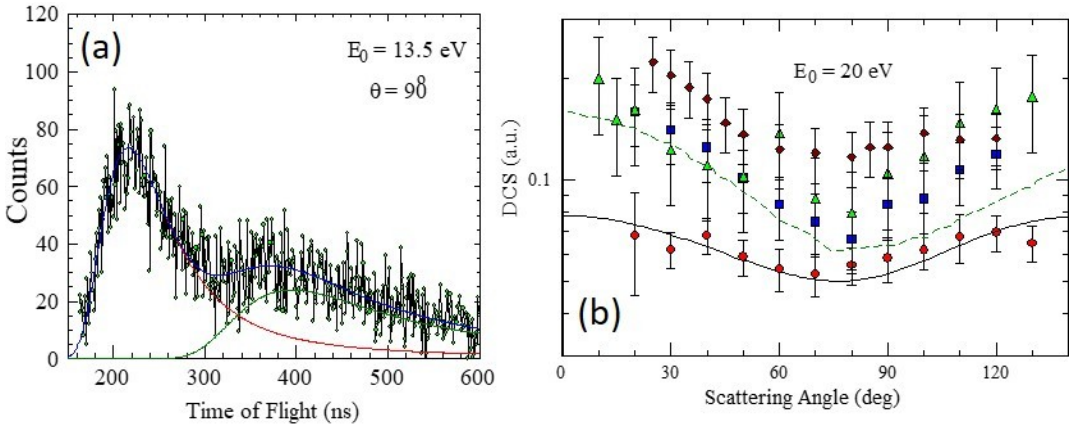

Fig. 5 Electron-impact excitation scattering DCS values for two excitation states of CO at electron impact energy (E_0) of 15 eV. (a) the X $^1\Sigma_g^+ \rightarrow a^3\Pi$ valence transition obtained from the experiments using energy-loss spectrometer (red circle) and using TOF (black square, blue triangle, green diamond), and computed using URKMol+ B-spline Model A (red dashed curve), URKMol+ B-spline Model B (black curve), UKRMol model without B-spline (green dashed curve), and SMC model (blue dashed curve) (For details, see [56]. (b) the X $^1\Sigma_g^+ \rightarrow B^1\Sigma^+$ Rydberg transition obtained from the experiments (red circle, blue triangle), and computed using URKMol+ 7330 (red dashed curve), URKMol+ 9440 (black curve), UKRMol model (green dashed curve) (For details, see [62]. Both panels reproduced with permission of IOP Publishing.

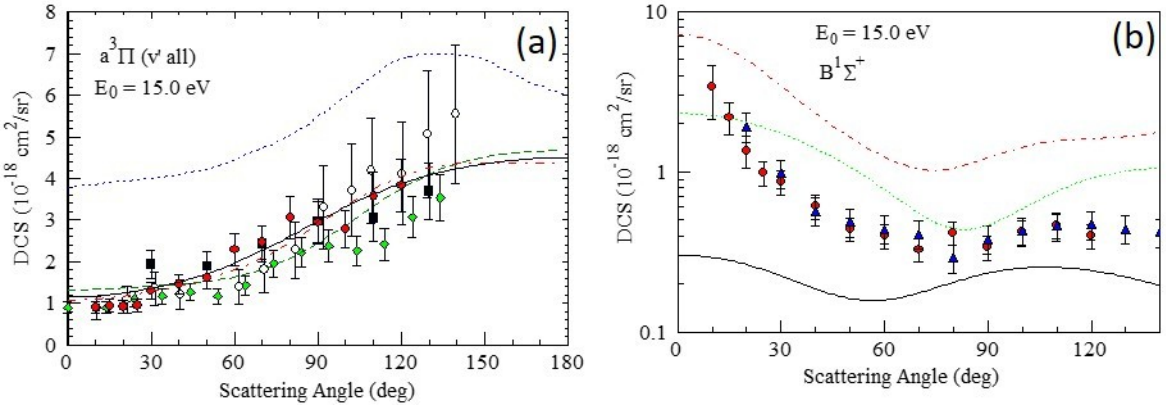

Fig. 6 (a) Ratio r′′ for Kr taken at electron impact energy (E_0) of 11.5 eV as a function of scattering angle; recent experimental work (red circle) and DSBR-31 calculation (solid curve) (For details, see [63]). (b) Elastic electron scattering DCS values at E_0 of 20 eV a function of scattering angle for $CHCl_3$ obtained from two experiments (red circle and black square) and calculated by SMC SEPP (black curve) and MCOP (dashed blue curve) theories (For details, see [67]). Reprinted with permission from Ref. [67]. Copyright (2019) by the American Physical Society.

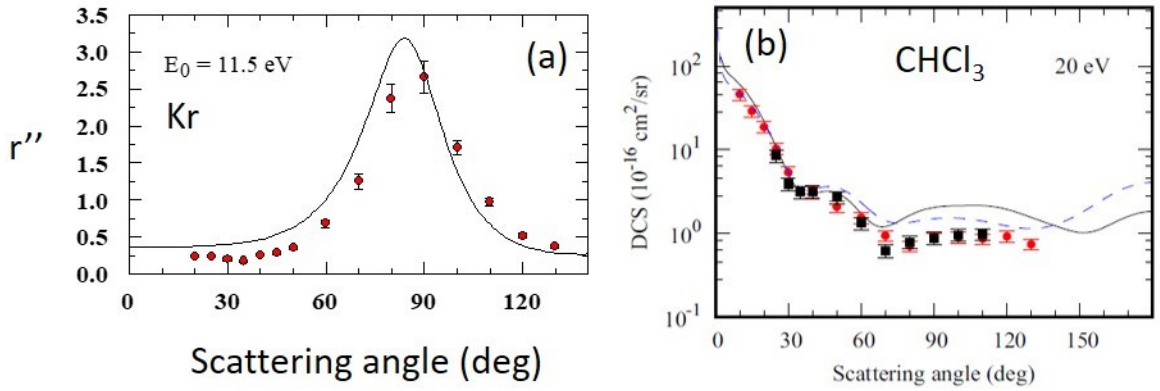

Fig. 7 Reaction microscope momentum imaging of DEA to formamide for two anionic fragments. Measured H^- (a) momentum and (b) angular distributions for electron impact at 10.5 eV, and NH_2^- (c) momentum and (d) angular distributions for electron impact at 5.3 eV. The black and the blue dot-dashed curves in panel (d) are angular distributions of NH_2^- calculated for Feshbach resonances of A'' and A' symmetry, respectively. The green dashed curve shows the result for the A' resonance with a 30° rotation of the dissociation axis to larger O-C-N angles. The incident electron direction is indicated by the vertical arrow in each panel. From Ref. [101].

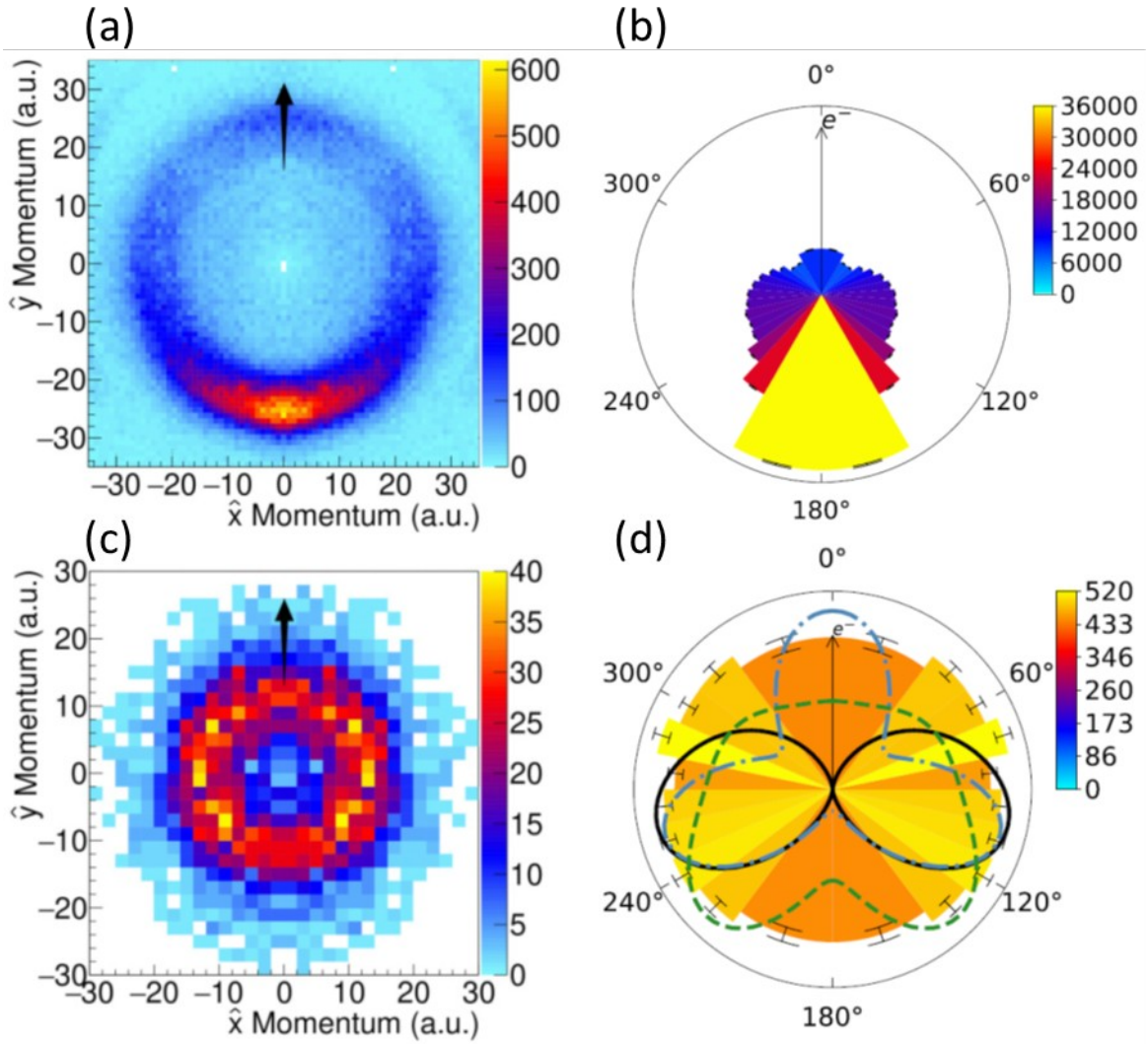

Fig. 8 Velocity slice imaging of anionic fragments from chlorinated hydrocarbons. Measured Cl^- (a) velocity slice ion image for 1.3 eV electron attachment to vinyl chloride, and (b) angular distributions for the same and two other energies on the same DEA resonance. Measured Cl^- (c) velocity slice ion image for 1.1 eV electron attachment to allyl chloride, and (d) angular distributions for the same and two other energies on the same DEA resonance. The incident electron direction (0^o) is indicated by the horizontal red arrow on the velocity slice images. Reprinted with permission from [105]. Copyright (2021) by the American Physical Society.

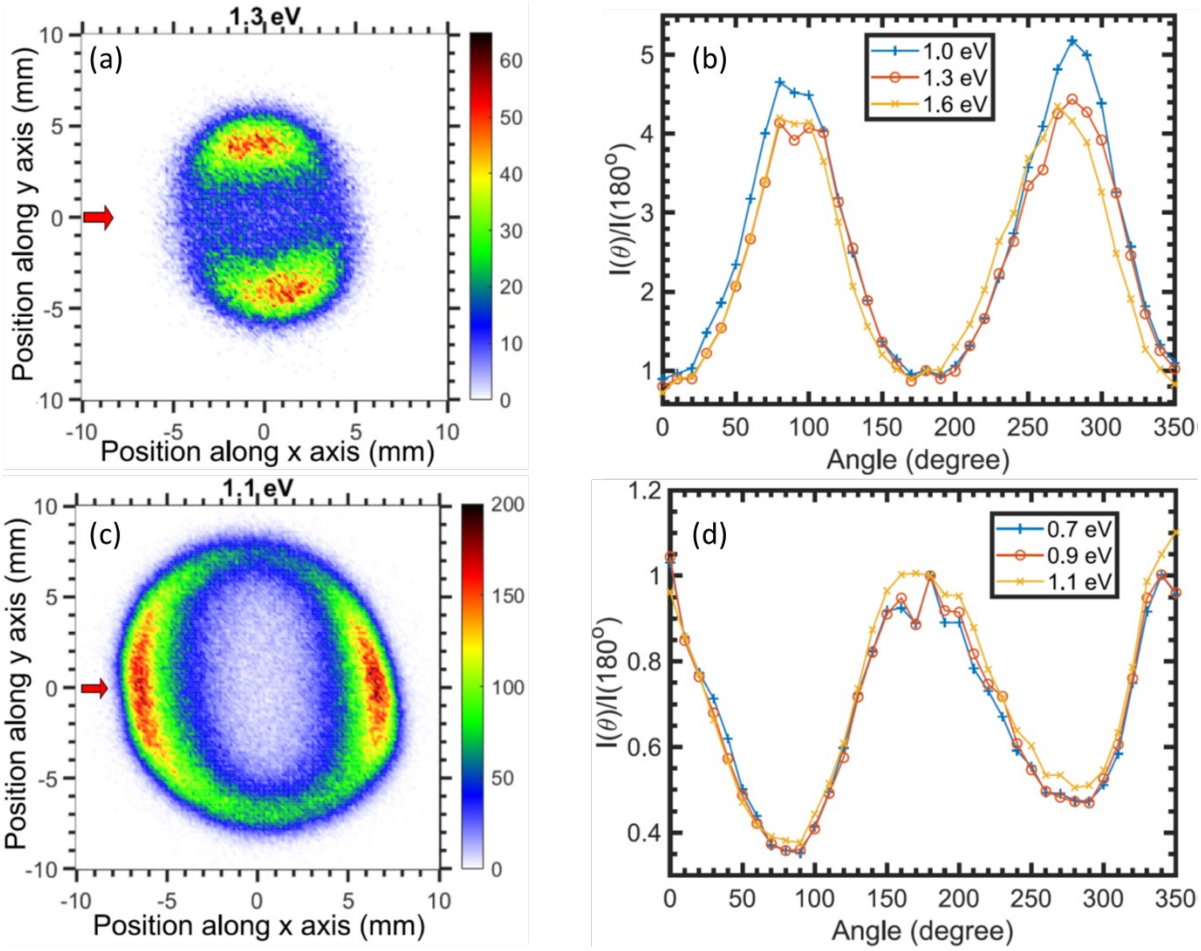

Fig. 9 (a) Electron – ion coincidence momentum imaging apparatus for electron impact ionization of molecules, from Ref. [106]. (b) Ion-ion coincidence TOF map of products formed by electron-impact double ionization of water-THF dimers. The diagonal lines mark the correlated TOF of the dimer fragments $H_2O^+ + C_4H_8O^+$ (solid diagonal line) and $H_2O^+ + C_4H_7O^+$ (dashed diagonal line). Most of the coincidence counts along the horizontal and vertical lines show no correlation between the ion times of flight, which is characteristic of false coincidence counts of two ions from different ionization events. Reprinted by permission from Springer Nature from Ref. [100], copyright (2018).

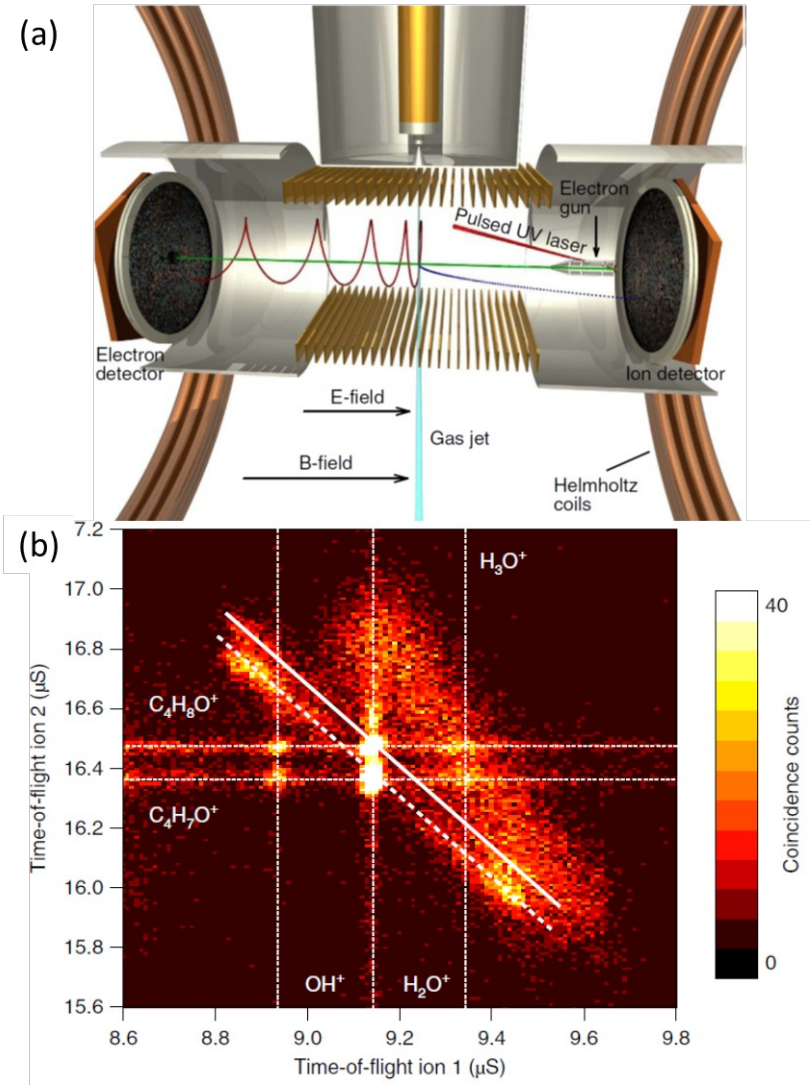

Fig. 10 (a) Schematic diagram of double chamber ion source used in the past for neutral (radical) products from electron collision with water vapor. Reprinted with permission from [115]. Copyright (1970) American Chemical Society. (b) Schematic diagram of the recent experimental setup and (c) the procedure steps of measurements of neutral detection from DEA to CCl_4 at the electron energy near 0 eV. Both panels reprinted with permission from [109]. Copyright (2017) by the American Physical Society.

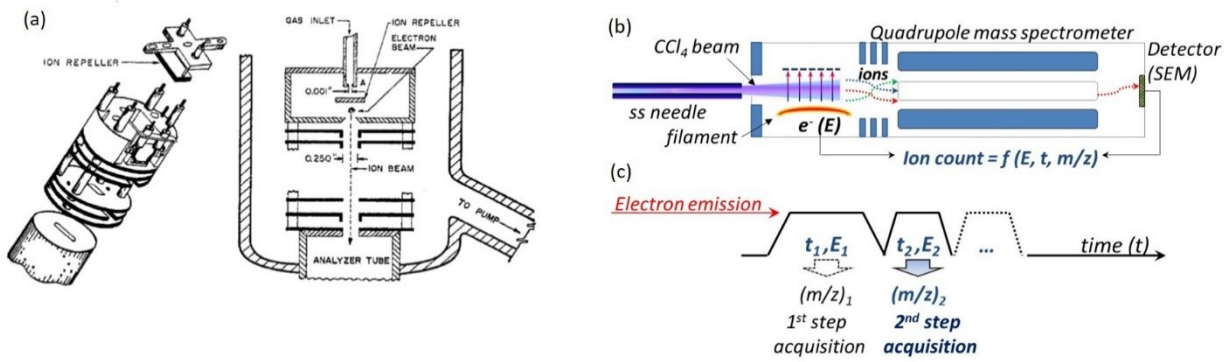

Fig. 11 Ion yield of Cl^- from the one-step acquisition (blue curve) in which Cl^- is formed directly from DEA to CCl_4 and ion yield of CCl_3^+ from the two-step acquisition, in which in the first step (E_1), CCl_3 is formed from DEA and in the second step, the neutral CCl_3 is ionized by electron impact of 11 eV (red circle). Both yields are as a function of the first-step incident electron energy (E_1). Two steps E_1 and E_2 correspond to steps in the experimental procedure presented in Fig. 13(c). Reprinted with permission from [109]. Copyright (2017) by the American Physical Society.

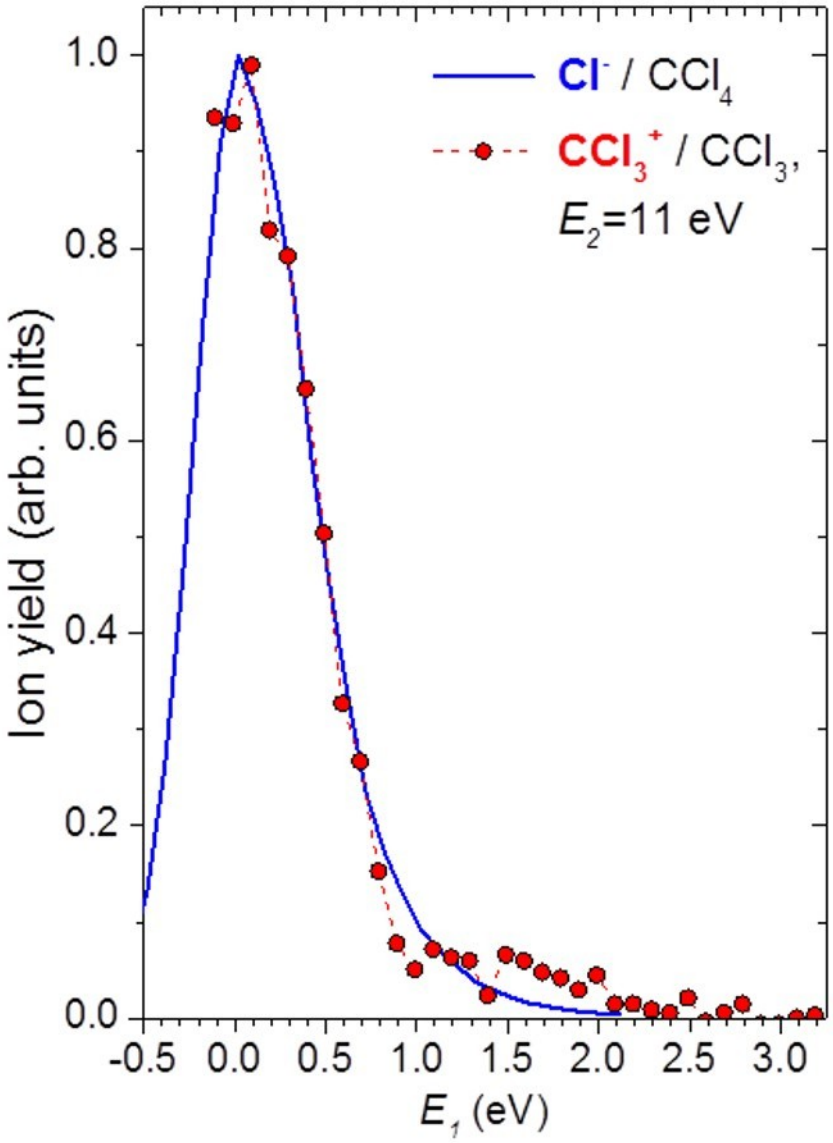

Fig. 12 Scheme of the experimental setup used to study electron attachment to micro-hydrated pyrimidine [151]. It consists of the homemade cluster source, which has been coupled to a double-focusing sector-field mass spectrometer. The most important components of the mass spectrometer are the ion source, the magnetic analyzer (B-sector), the energy analyzer (E-sector) and the secondary electron multiplier (SEM). Reprinted with permission Ref. [151]. Copyright (2017) American Chemical Society.

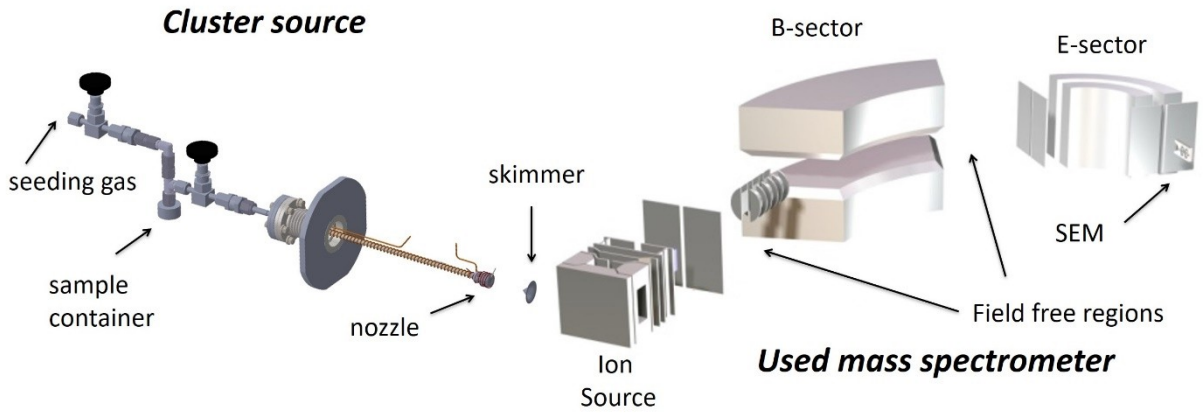

Fig. 13 Ion yield ratio of the NO_2^- fragment and $NIMO(H_2O)_n^-$ corresponding to the undissociated NIMO parent anion with attached water molecules. The ratio is plotted as a function of the mean number <n> of water molecule in the neutral clusters. Taken from [159].

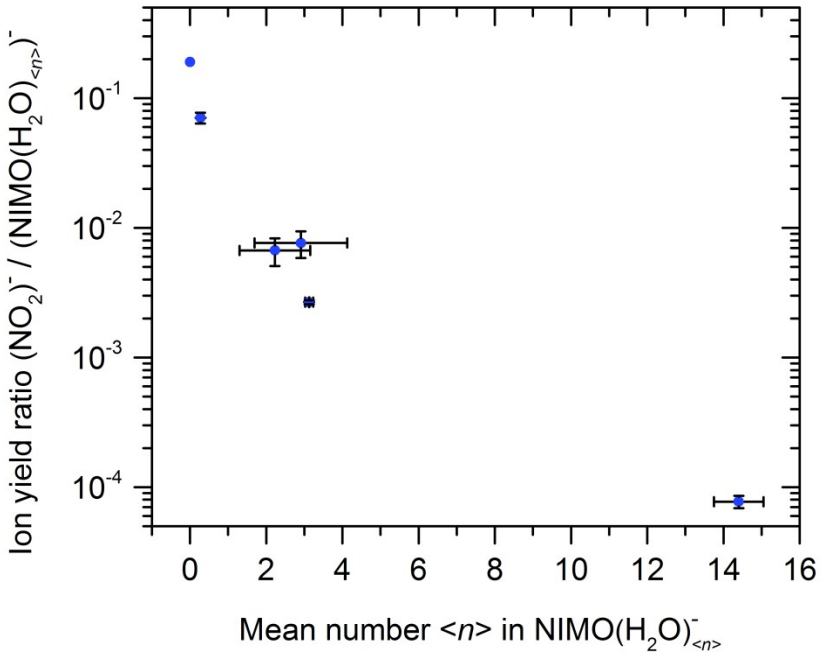

Fig. 14 (a) Ion yield ratio of the NO_2^- fragment and $MISO(H_2O)_n^-$ corresponding to the undissociated MISO parent anion with attached water molecules (blue square). Ion yield ratio of the $(H_2O)_jOH^-$ fragment anion and $MISO(H_2O)_n^-$, corresponding to the anionic products with attached water molecules (red circle). Both ratios are plotted as a function of the mean number <n> of water molecule in the neutral clusters. (b) Computed reaction energies for the respective DEA channels, $MISO^-(H_2O)_n \rightarrow NO_2^-(H_2O)_n$ + (MISO - NO_2), reaction (1), and $MISO^-(H_2O)_n \rightarrow OH^-(H_2O)_n$ + (MISO - OH), reaction (2), as a function of the number n of water molecules (for computational details, see [160]). Both panels taken from [160].

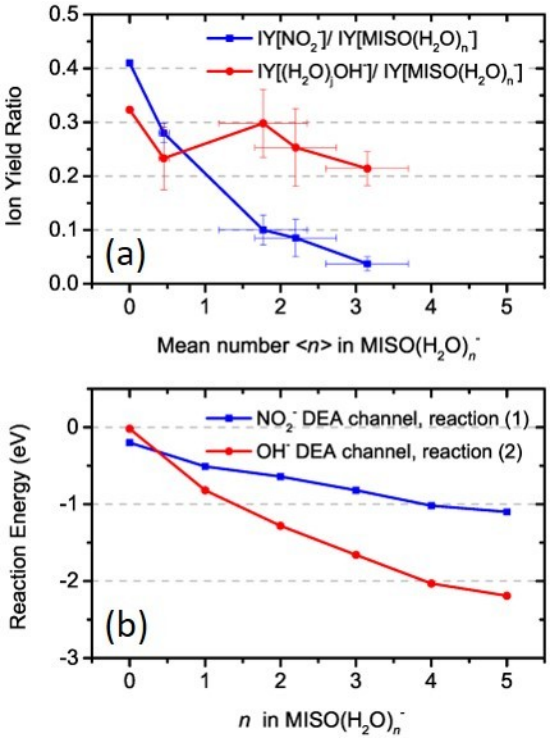

Graphical Abstract